Results in Physics 18 (2020) 103292

Contents lists available at ScienceDirect

Results in Physics

journal homepage: www.elsevier.com/locate/rinp

A mutual coupled concentric crossed-Line split ring resonator (CCSRR) based epsilon negative (ENG) metamaterial for Tri-band microwave applications

Mohammad Shahidul Islam[a,*], Mohammad Tariqul Islam[a,*], Norsuzlin Mohd Sahar[b], Hatem Rmili[c], Nowshad Amin[d], Muhammad E.H. Chowdhury[e]

[a] Department of Electrical, Electronic and Systems Engineering, Universiti Kebangsaan Malaysia, Bangi 43600, Selangor, Malaysia
[b] Space Science Center (ANGKASA), Institut Perubahan Iklim (IPI), Universiti Kebangsaan Malaysia, Bangi 43600, Selangor, Malaysia
[c] King Abdulaziz University, Faculty of Engineering, Electrical and Computer Engineering Department, P.O. Box 80204, Jeddah 21589, Saudi Arabia
[d] Institute of Sustainable Energy, Universiti Tenaga Nasional, Kajang 43000, Malaysia
[e] Department of Electrical Engineering, Qatar University, Doha 2713, Qatar

ARTICLE INFO

Keywords:
SRR
Metamaterial
Mutual coupling
Microwave application

ABSTRACT

A metamaterial design and its analysis based on an epsilon negative concentric crossed-line split ring resonator (CCSRR) have been presented in this paper. The CCSRR unit cell structure is the amendment of the typical concentric split ring resonator (CSRR). The inserted crossed line increases the electrical length of the presented CCSRR unit cell. The dimension of the proposed CCSRR unit cell is $10 \times 10 \times 1.575$ mm^3 and it is printed on the Rogers RT 5880 substrate material. The transmission frequency ranges from 6.33 GHz to 6.65 GHz, 10.42 GHz to 10.73 GHz, and 13.21 GHz to 13.42 GHz which covers the frequency bands of C, X, and Ku-band of microwave applications. A complete analysis of scattering parameters, effective medium parameters, mutual coupling effect as well as the unit cell characteristics with electromagnetic analysis have been performed in this study. The proposed CCSRR unit cell structure exhibits epsilon negative characteristics in the frequency ranges of 6.53 GHz to 6.96 GHz, 10.63 GHz to 10.91 GHz, and 13.37 GHz to 13.40 GHz. Experimental validation has also been performed by measuring the scattering parameters of the proposed CCSRR unit cell and its array structure. Furthermore, the capacitive coupling among the concentric split ring resonators within the 1×2 and 2×2 array structures have been studied which is based on the near field split gaps that lead to the fundamental inductive-capacitive resonances. Besides, the effective medium ratio 4.5 implies the effectiveness and compactness of the proposed CCSRR unit cell structure. The compactness, effective medium parameters, and effective medium ratio make the proposed CCSRR metamaterial appropriate for the microwave applications.

Introduction

Electromagnetic material development and applications are increasing dramatically over these years, which led to the development of metamaterials. Metamaterials are artificially engineered novel and synthetic materials which have unique electromagnetic properties not found in nature. The properties depend on the metamaterial shape, size, orientation, and arrangement of the inclusion. The unique properties of the metamaterials such as electric and magnetic resonance, cloaking, etc. allow us to define them as left-handed metamaterials that can be classified as single negative and double negative metamaterials. In addition, it is notable that single negative metamaterials can be categorized into two groups: if the real part of the permittivity is negative and permeability in positive, that is called Epsilon-negative (ENG) metamaterial, and if the real part of the permittivity is positive and permeability in negative, that is called Mu-negative (MNG) metamaterial. Split ring resonators (SRR) form these left-handed negative-index metamaterials that also identify the resonance frequency with its geometrical structure. This SRR also leads to the microwave frequency range with simultaneous effective medium parameters. The results of capacitive and inductive effects and the SRR resonance phenomenon happens because of the interaction of the metallic and electromagnetic fields. Researches have been performed nowadays about the SRR and its applications through ENG or MNG metamaterial characteristics [1–4]. A new D-Z shaped SRR based SNG metamaterial has been presented and investigated for triple bands of L-band, S-band, and X-band applications

* Corresponding authors.
E-mail addresses: P97645@siswa.ukm.edu.my (M. Shahidul Islam), tariqul@ukm.edu.my (M.T. Islam).

https://doi.org/10.1016/j.rinp.2020.103292
Received 8 June 2020; Received in revised form 15 July 2020; Accepted 24 July 2020
Available online 08 August 2020

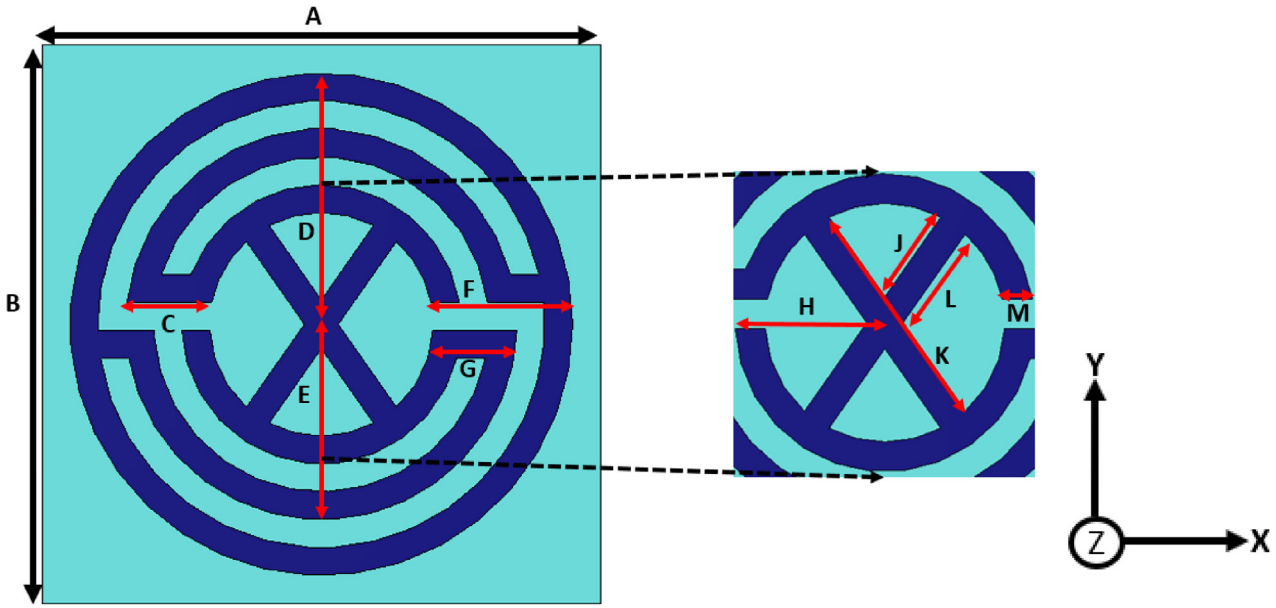

Fig. 1. Proposed CCSRR Unit Cell Structure (Top View).

Table 1
Parameters of the proposed CCSRR unit cell structure.

Substrate Length, A	**E**	**J**
10 mm	3.5 mm	1.65 mm
Substrate Width, B	**F**	**K**
10 mm	2.5 mm	3.95 mm
C	**G**	**L**
1.5 mm	1.5 mm	1.8 mm
D	**H**	**M**
4.5 mm	2.5 mm	0.5 mm

[2]. A novel dual-band nonconcentric delta loop resonator-based metamaterial is presented and analyzed at [5] within the single and double negative region that can be applied for several potential microwave applications.

Double split ring resonator (DSRR) based epsilon negative metamaterial has been presented at [6] for the microwave imaging applications. This DSRR has the concentric inverted splits that exhibit the epsilon negative characteristics and enhance the bandwidth. A modified H-shape split ring resonator has been presented at [7] where it has the Z-axis wave propagation and has the C-band transmission spectra of microwave applications. Single split circle ring metamaterial with lumped resistor has been presented at [8] for the X-band microwave applications. A crossed loop resonator-based dual-band epsilon negative and near-zero metamaterial has been presented at [9] where this crossed loop resonator has an impact on low-impedance characteristics. Adjustable graphene epsilon near zero metamaterial has been presented at [10] for the radio frequency range where the negative permittivity moderates the carrier concentration of the conductive networks. A hexagonal-shaped SRR based metamaterial has been presented at [11] for dual-band S, and X-band microwave applications. The analysis also shows the mutual coupling effect of the intercell structures. A complementary SRR based metamaterial has been presented at [12] which has a good effective medium ratio that makes it applicable for C-band microwave applications. A modified RLC-based split ring resonator has been presented at [13] a tunneling structure is presented that increases the negative refractive index bandwidth of 3.40 GHz. This modified SRR is applicable for the X-band of microwave region. Besides, multi SRR based metamaterial is presented at [14] to reduce the absorption rate that was exposed to the human head and mobile phone interaction. This SRR based metamaterial is for L-band and S-band microwave applications. A U-joint double split-O shaped split-ring resonator based metamaterial is presented at [15] which works as an absorber and applicable for X-band and Ku-band applications. The effective medium of this metamaterial structure is 4.5. Another left-handed SRR based metamaterial is presented at [16] which is applicable for the C-band and Ku-band satellite applications. A planar chiral metamaterial is presented at [17] where it is constructed by Fermat's spiral structure resonator. The structure has a higher Q-factor and applicable for triband applications. An anisotropic metamaterial is presented at [18] which has high efficient circular polarization and applicable for dual-band microwave application. A meander wire structure loaded resistor based metamaterial is presented at [19] which has a wide angular range on TE and TM modes of the electromagnetic wave propagation. An asymmetric sectional resonator-based metamaterial is presented at [20] for broadband microwave applications where the structure exhibits an angle insensitivity for both TE and TM modes. A single resonator structure-based metamaterial is presented at [21] which is polarization insensitive and applicable for microwave applications. Another polarization insensitive metamaterial is presented at [22] which is applicable for detection, sensing, and stealth technology.

In addition, changes in the relative orientation of the SRRs with each other or the intercell distance among each other is the prominent way to tune the metamaterial resonance frequency [11,23]. It has been a research topic nowadays to analyze the intercell coupling effects that help to enhance bandwidth or absorption through a different orientation of the metamaterials [24,25]. Inductive-capacitive (LC) resonances with a long-range radiative coupling have been shown at [26] and for high-order resonance at [27]. The coupled resonance quality factor is enhanced by an extreme reduction in radiation dumping and the long-range of this diffractive coupling happens by the cross-section periodicity of the SRR array. This structure matches the fundamental inductive-capacitive resonances or high order resonances for wavelength of incident light.

In this paper, a metamaterial based on concentric crossed line split ring resonator (CCSRR) has been proposed for the C, X, and Ku-band microwave applications. The proposed CCSRR unit cell structure has the epsilon negative metamaterial characteristics with complex refractive index values. The single negative region has been found from 6.51 GHz to 6.67 GHz, 10.65 GHz to 10.90 GHz, and 13.32 GHz to 13.42 GHz, respectively. There is also an analysis of the 1×2 and 2×2 CCSRR unit cell array structures and their effective medium

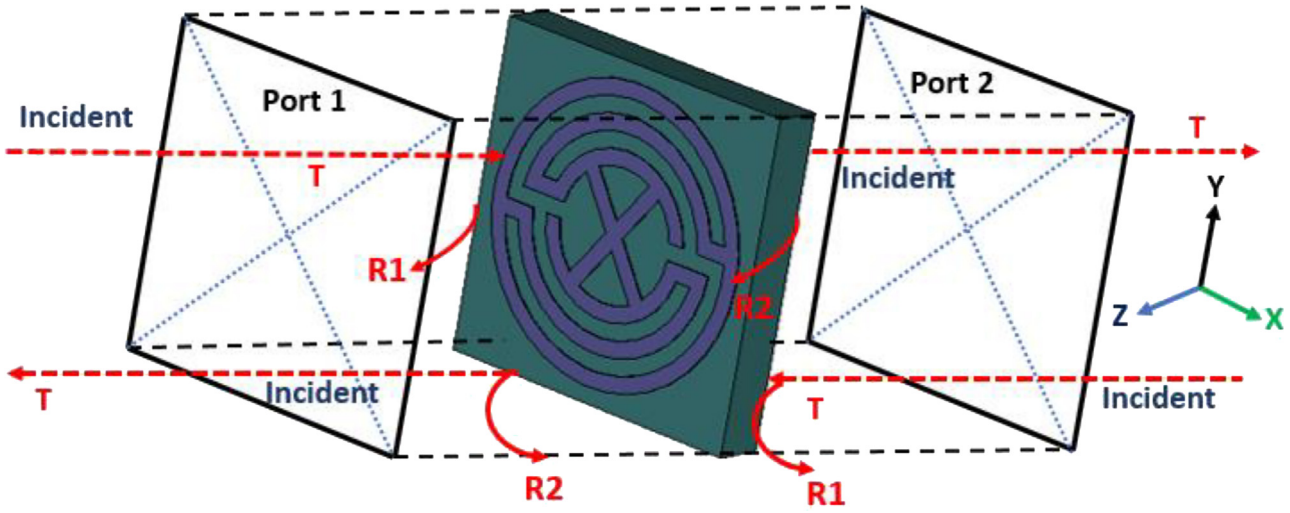

Fig. 2. Boundary condition of the proposed CCSRR unit cell structure with incidence, reflection, and transmission.

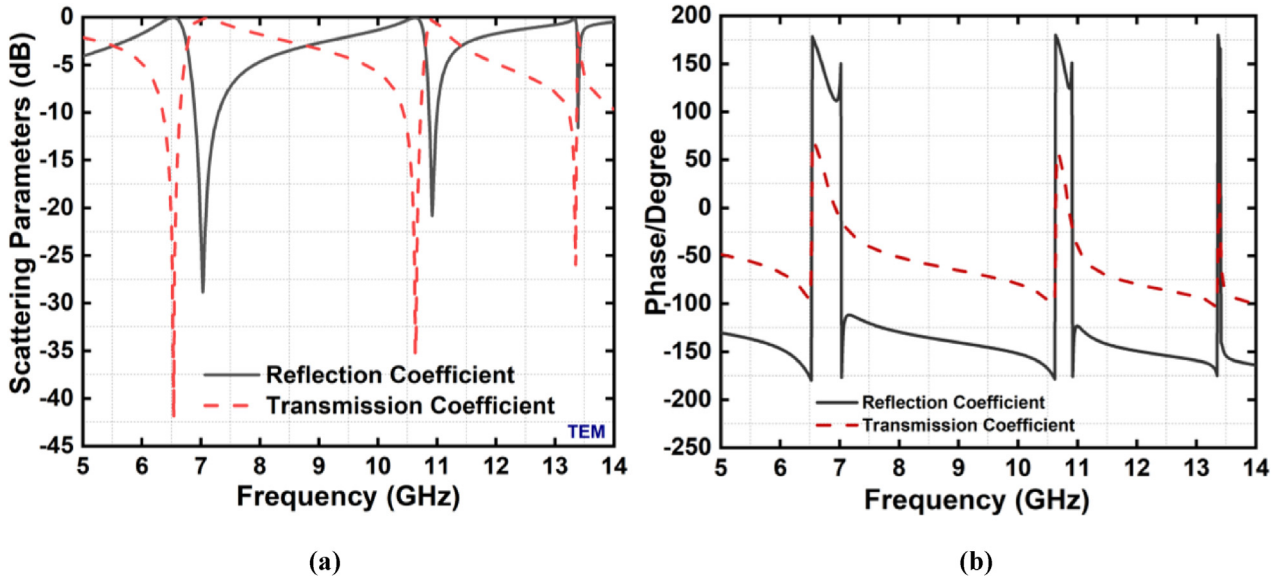

Fig. 3. (a) Scattering Parameters TEM Mode (b) Phase (c) Scattering Parameters TE Mode (d) Scattering Parameters TM Mode (e) Effective Permittivity (f) Effective Permeability (g) Effective Refractive Index (h) Normalized Real and Imaginary Impedance (i) Overall Normalized Impedance.

parameters. In addition, the mutual coupling effect among the CCSRR unit cell structures has also been presented in this paper. The effective medium ratio of the proposed CCSRR is 4.5 the defines compactness and acceptability.

Design procedure of the CCSRR unit cell structure

The proposed concentric crossed line split ring resonator (CCSRR) unit cell structure is presented in Fig. 1 where it contains the top view of the proposed CCSRR unit cell structure. The proposed CCSRR unit cell structure is a modification of the conventional concentric split ring resonators. To design and analyze the properties of the proposed CCSRR unit cell structure, Frequency domain-based electromagnetic simulation software CST has been used. Initially, the conventional SRR has been drawn where two concentric metal rings are separated by a gap and having splits on both opposite sides. The proposed CCSRR structure consists of a perfect electric conductor (PEC) which is printed on the Rogers RT5880 substrate material and that creates electromagnetic radiation and matches the impedance. The dielectric constant of the substrate material is 2.2 where the loss tangent is 0.009. The thickness of the substrate and PEC are 1.575 mm and 0.035 mm, respectively which are responsible to create the capacitance and inductance by fixing the resonance frequency. The design specification of the proposed CCSRR unit cell structure is illustrated in Table 1.

Effective medium parameters of the proposed metamaterial

The electromagnetic field interaction with the metallic inclusions, their placements and distributions play a very important role in the characterization of a metamaterial structure. The orientation on the specific direction of the electric and magnetic field enhances the effective parameters like permittivity and permeability. In addition, the tangent inclusions of the electric field and the normal direction of the magnetic field to the surface structure also enhance the effective parameters. Thus, during the characterization procedure, the electromagnetic field distribution must be specified accurately. To get the ideal electromagnetic field, the boundary conditions are set in the two axial directions; X-direction and Y-direction, respectively.

The CCSRR unit cell structure's responses are directed by those characteristics. The upper and lower walls of CCSRR with the

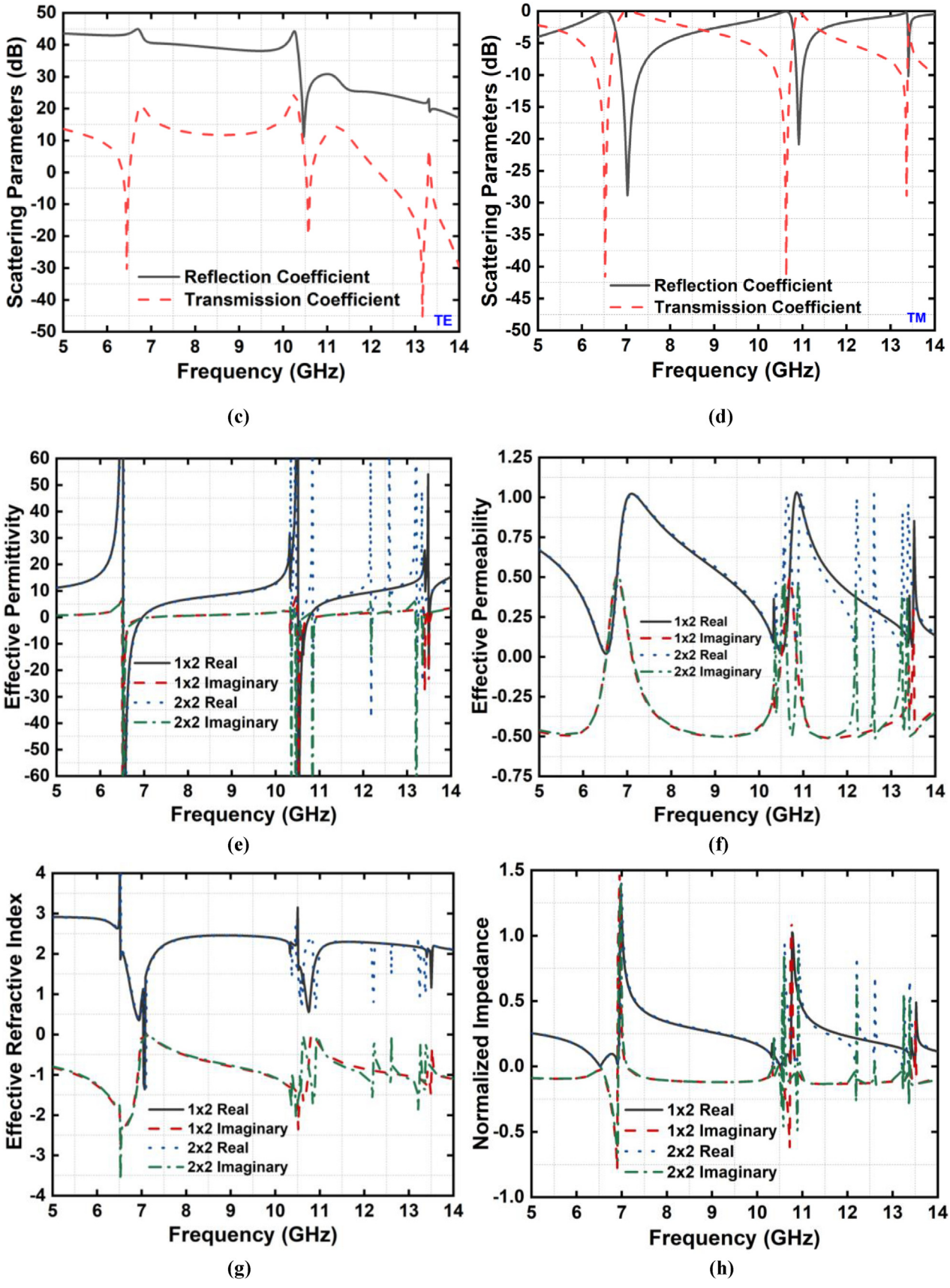

Fig. 3. (*continued*)

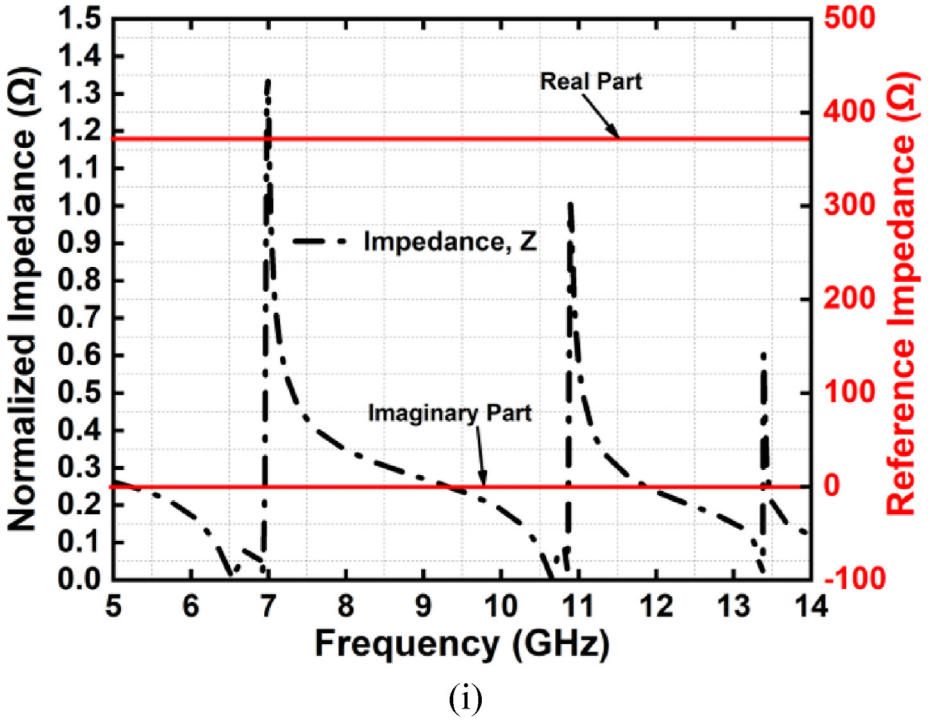

(i)

Fig. 3. (*continued*)

Table 2
Frequency ranges of effective parameters of the proposed CCSRR unit cell structure.

Real Parameter	Resonance Frequency	Imaginary Parameter	Resonance Frequency
Negative Permittivity	6.51 GHz–6.67 GHz, 10.65 GHz–10.90 GHz, 13.32 GHz–13.42 GHz	Negative Permittivity	6.51 GHz–7.04 GHz, 10.60 GHz–11.19 GHz, 13.30 GHz–13.46 GHz
Positive Permeability	6.53 GHz, 10.62 GHz, 13.34 GHz	Positive Permeability	6.53 GHz–7.11 GHz, 10.62 GHz–10.99 GHz, 13.34 GHz–13.42 GHz
Refractive Index (Negative)	7.08 GHz	Refractive Index (Positive)	6.54 GHz, 10.66 GHz
Refractive Index (Positive)	10.86 GHz, 13.39 GHz	Refractive Index (Negative)	13.36 GHz

perpendicular form to E-vector and back and front walls of CCSRR with the perpendicular to H-vector have been applied with the open add boundaries to operate the free space. Negative Z-axis and positive Z-axis are used as the waveguide ports position and the CCSRR unit cell structure is placed in between them which is later energize towards the Z-axis by the electromagnetic wave. Fig. 2 represents the boundary condition of the proposed CCSRR unit cell structure with incidents, reflection, and transmission. There are two slabs to be considered for reflection coefficients; one is air to MTM slab and the other is MTM slab to air. The transmission coefficients are the same in both direction and a plane wave is propagating in the air is the incident from either side. This process helps to observe the field features of the resonance frequencies by joining the magnetic, electric, and open space conditions of each wall. The simulation procedure of the proposed CCSRR structure has been performed with a Frequency-domain solver where the tetrahedral meshing is applied within the frequency range of 5 GHz to 14 GHz.

To extract the effective medium parameters from the simulation data, the Nicolson-Ross-Weir (NRW) method is used which is one of the popular methods of electromagnetic characterization techniques [28]. The following equations are used to extract the effective parameters.

$$S_{11} = \frac{(1 - Z^2)T}{1 - T^2Z^2} \tag{1}$$

$$S_{21} = \frac{(1 - T^2)Z}{1 - T^2Z^2} \tag{2}$$

$$\varepsilon_r = \frac{2}{jk_0d}\frac{1 - S_{21} + S_{11}}{1 + S_{21} - S_{11}} \tag{3}$$

$$\mu_r = \frac{j2S_{11}}{jk_0d} + \mu_0 \tag{4}$$

$$\eta_r = \frac{2}{jk_0d}\sqrt{\frac{(S_{21} - 1)^2 - S_{11}{}^2}{(S_{21} + 1)^2 - S_{11}{}^2}} \tag{5}$$

The representations: the interface reflection coefficient, **T**, the reflection and transmission coefficient $\mathbf{S_{11}}$, and $\mathbf{S_{21}}$, the permittivity, permeability, and refractive index ε_r μ_r, and η_r respectively, the wavenumber $\mathbf{K_0}$ and the thickness of the substrate **d**.

Fig. 3(a) represents the reflection and transmission coefficient of the proposed CCSRR unit cell structure. Fig. 3(b) represents the phase of the CCSRR unit cell. The standard scattering parameter is set −10 dB. The frequency ranges of the reflection coefficient are 6.90 GHz to 7.29 GHz, 10.86 GHz to 11.00 GHz, and 13.36 GHz to 13.43 GHz, respectively. The frequency ranges of the transmission coefficient are 6.34 GHz to 6.62 GHz, 10.43 GHz to 10.73 GHz, and 13.22 GHz to 13.39 GHz, respectively. Different boundary conditions are chosen to analyze the TE and TM mode of the proposed CCSRR unit cell structure. Fig. 3(c) and (d) represents the scattering parameters of the proposed CCSRR unit

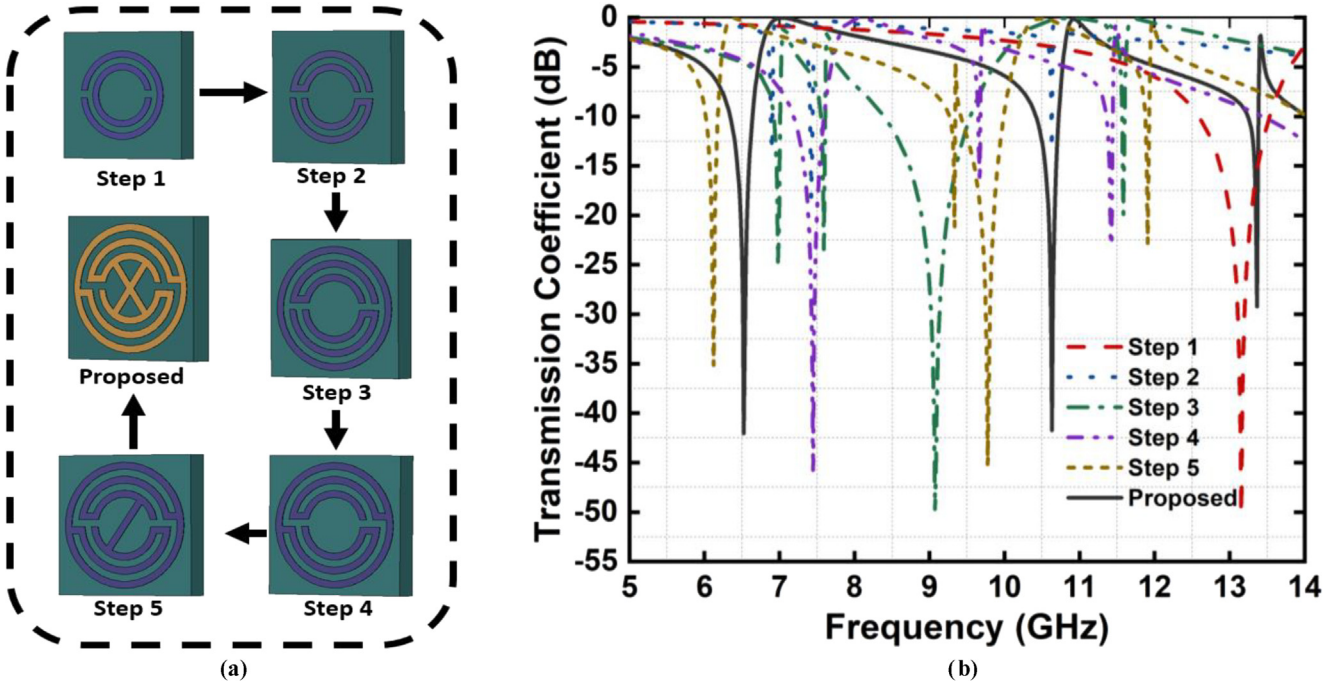

Fig. 4. Evolution of the Proposed CCSRR Structure (a) Design Steps (b) Transmission Coefficient.

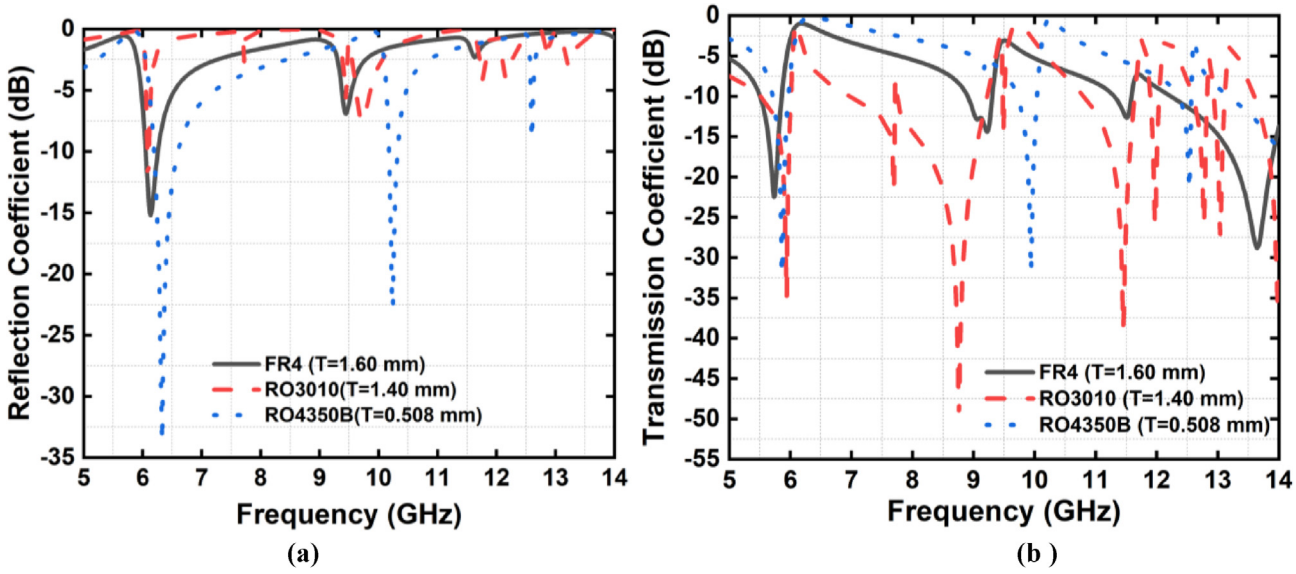

Fig. 5. Scattering Parameters Analysis on Different Dielectric Substrates (a) Reflection Coefficient (b) Transmission Coefficient.

cell structure on TE and TM mode. It is noticeable that the resonance is mainly imaginary for the TE mode simulations whereas the TM mode and TEM mode has the same resonance, frequency bands. Fig. 3(e), (f), and (g) are the real and imaginary permittivity, permeability, and refractive index respectively. The negative real permittivity frequency ranges are 6.51 GHz to 6.67 GHz, 10.65 GHz to 10.90 GHz, and 13.32 GHz to 13.42 GHz, respectively. The real permeability of the proposed CCSRR unit cell structure shows positive real permeability. The lowest value is 0.10 for the three-resonance frequency of 6.53 GHz, 10.62 GHz, and 13.34 GHz, respectively. The real refractive index has the complex value in three resonance frequencies where 7.08 GHz resonance point shows the value −1.41, 10.86 GHz resonance point shows the value +0.51, and 13.39 GHz resonance point shows the value +1.12, respectively. The imaginary resonance frequency points are 6.54 GHz, 10.66 GHz, and 13.36 GHz where the containing values are −4.00, 2.20, and −1.5, respectively. The normalized frequency points of 6.97 GHz and 10.87 GHz show the impedance 1.00 Ω where the normalized impedance is 0.61 Ω at 13.38 GHz which is shown in Fig. 3(h). The imaginary normalized values are 0.97 Ω, 1.00 Ω, and 0.33 Ω for the frequency points of 6.97 GHz, 10.87 GHz, and 13.38 GHz, respectively. The overall normalized impedance and reference impedance are shown in Fig. 3(i). The frequency ranges of the effective parameters are stated in Table 2. The analysis shows that the real values are negative for the permittivity, positive for the permeability, and negative and positive for the refractive index within the same resonance frequency bands which indicates the proposed CCSRR unit cell shows the single negative metamaterial characteristics.

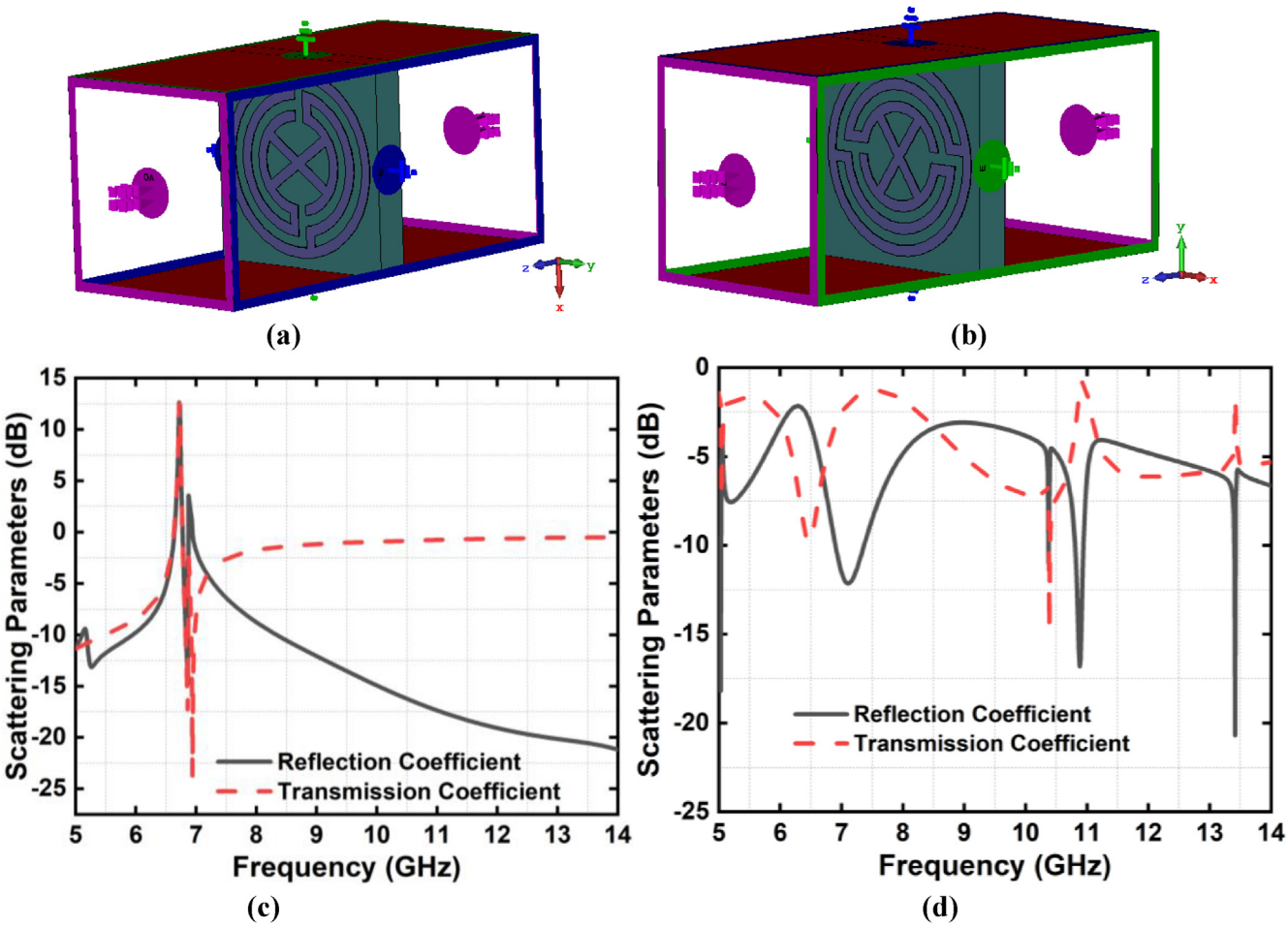

Fig. 6. Scattering Parameters Analysis on Different Port Signals (a) X-axis port **(b)** Y-axis port (c) Scattering parameters of X-axis port (d) Scattering parameters of Y-axis port.

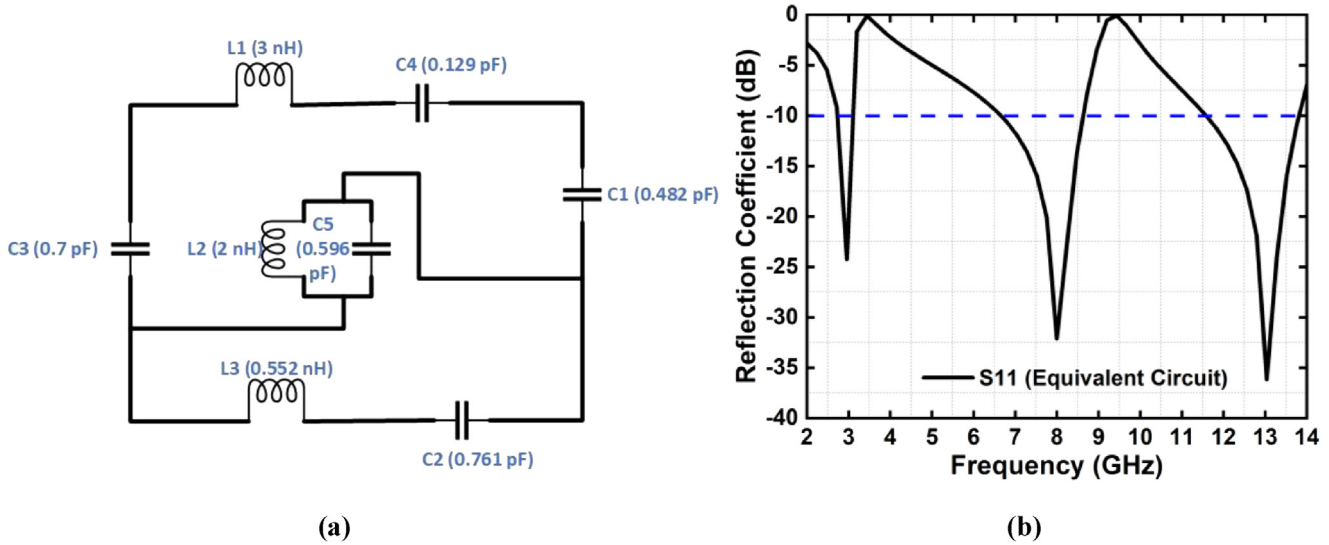

Fig. 7. (a) Equivalent Circuit and (b) Reflection coefficient of the proposed CCSRR unit cell equivalent circuit.

Evolution of the proposed CCSRR design structure

Several elements are needed to be considered for the multiband operating frequencies. By adjusting the dimensions of substrate thickness and conducting elements' structures, it is possible to tune the resonance frequency. As the highest electric field created from the split gaps of the CCSRR unit cell structure shows high capacitance and strong coupling, the inner radius, length, and width of ring and slots, split gaps and mutual coupling are also responsible for the multiband operating frequencies. The changes in the dielectric and boundary conditions increase or decrease the resonance frequency which can also be possible because of their losses.

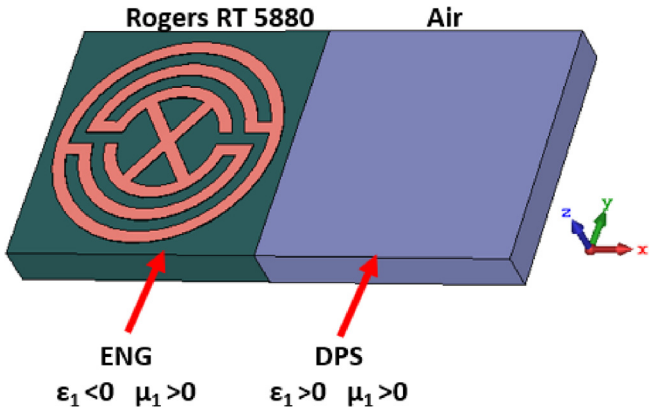

Fig. 8. ENG-DPS Slab.

In addition, the evolution of the proposed CCSRR unit cell structure is given in Fig. 4 where step 1 contains a double circular conducting line which is a conventional SRR and it continues to step 2 with modified splits into it. Step 1 shows the transmission frequency at 12.89 GHz where step 2 shows at 6.87 GHz, 7.39 GHz, and 10.63 GHz, respectively. Step 3 comes with another outer circular conducting line and it is connected to the other two circular conducting lines in step 4. Step 3 shows the transmission frequency at 6.96 GHz, 7.60 GHz, 9.08 GHz, and 11.57 GHz, respectively where the modification in step 4 transmits at 7.48 GHz, 9.66 GHz, and 11.41 GHz, respectively.

Modification of step 4 comes into step 5 where there is a straight conducting line added into the inner circular resonator and the transmission frequencies are 6.14 GHz, 9.32 GHz, 9.78 GHz, and 11.89 GHz, respectively. Finally, it comes to the proposed structure which is the modification of step 5 and it consists of another straight conducting line that makes the proposed structure a concentric crossed line structure. The transmission frequencies of the proposed CCSRR structure are 6.53 GHz, 10.63 GHz, and 13.35 GHz, respectively. The analysis shows that the proposed CCSRR covers the maximum frequency bands of C, X, and Ku-band, respectively whereas step 5 covers C-band and X-band. Step 2, step 3 and step 4 cover the C-band and X-band, respectively where step 1 covers only one transmission frequency at Ku-band. The proposed CCSRR unit cell structure has the maximum transmission frequency bands within 5 GHz to 14 GHz frequency regime.

Parametric studies of the CCSRR structure

The analysis is performed by using different substrate materials for the proposed CCSRR unit cell structure. Three different types of substrate materials excluding the proposed Rogers RT5880 with different thicknesses are used for this analysis. The substrate materials are FR4 with 1.60 mm thickness, Rogers RO3010 with 1.40 mm thickness, and Rogers RO4350B with 0.508 mm thickness, respectively. The reflection coefficient is shown in Fig. 5(a) states that FR4 and RO3010 have one resonance frequency band of 6.13 GHz where RO4350B has two frequency bands of 6.36 GHz and 10.25 GHz, respectively. Fig. 5(b) shows the transmission coefficient of different substrate materials. FR4 has two frequency bands of 5.73 GHz and 13.66 GHz where RO3010 has multiple resonance frequencies that indicate the transmission distortion. RO4350B has three resonance frequencies of 5.87 GHz, 9.83 GHz, and 12.55 GHz, respectively. In both reflection and transmission coefficient analysis, the standard scattering value is set −10 dB. Based on the analysis, it is noticeable that the proposed CCSRR unit cell structure has the maximum resonance frequencies in terms of the reflection coefficient. RO4350B shows the same resonance bands as the proposed CCSRR transmission bands but the bandwidth of the proposed CCSRR is higher which makes the proposed CCSRR unit cell structure more suitable for the Rogers RT5880 substrate material.

In addition, there has been another analysis of the different boundary conditions and port signals which is shown in Fig. 6. Fig. 6(a) and (b) represent the CCSRR unit cell structure with a port signal in the X-axis direction and Y-axis direction, respectively. The electric field and magnetic field are set in the Y-axis and Z-axis direction, consecutively, for the X-axis port signal and in the X-axis and Z-axis direction for the Y-axis port signal. Fig. 6(c) shows the reflection and transmission

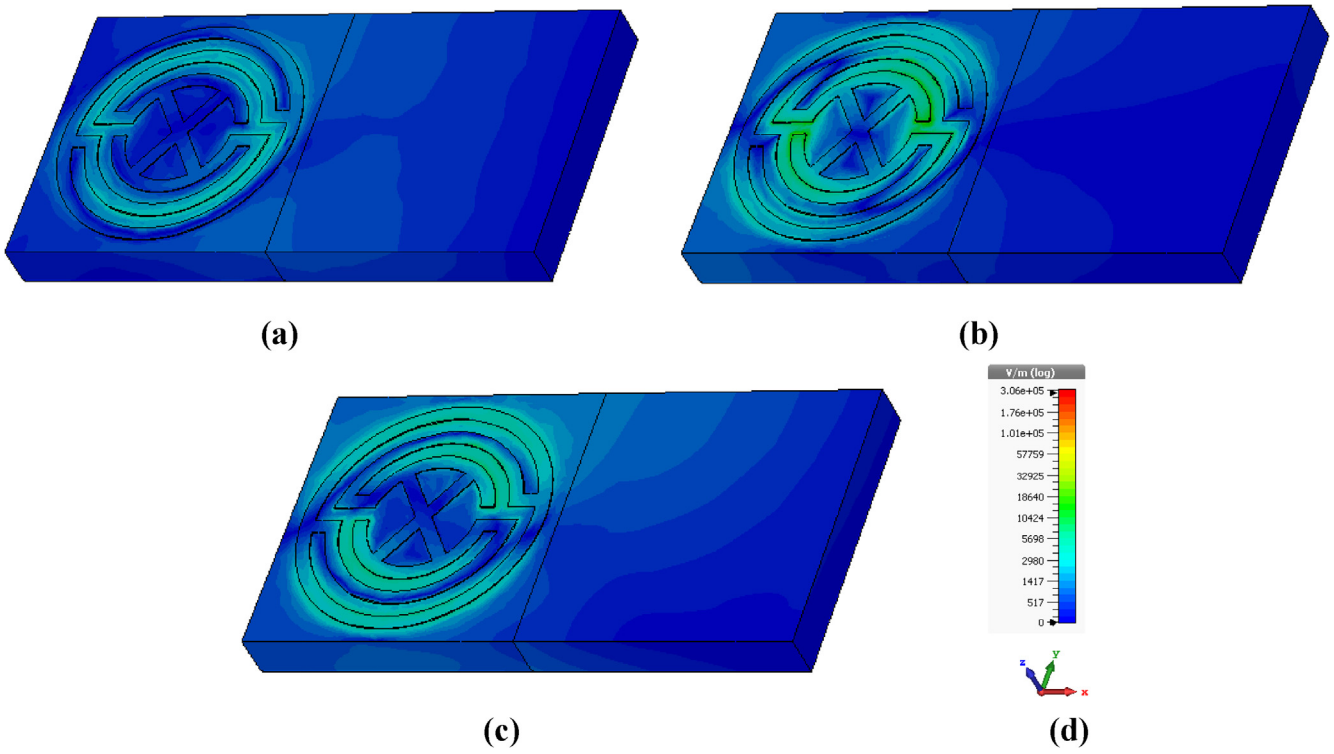

Fig. 9. Electromagnetic wave interaction on electric field (a) at 6.53 GHz (b) at 10.63 GHz (c) at 13.35 GHz (d) Scale.

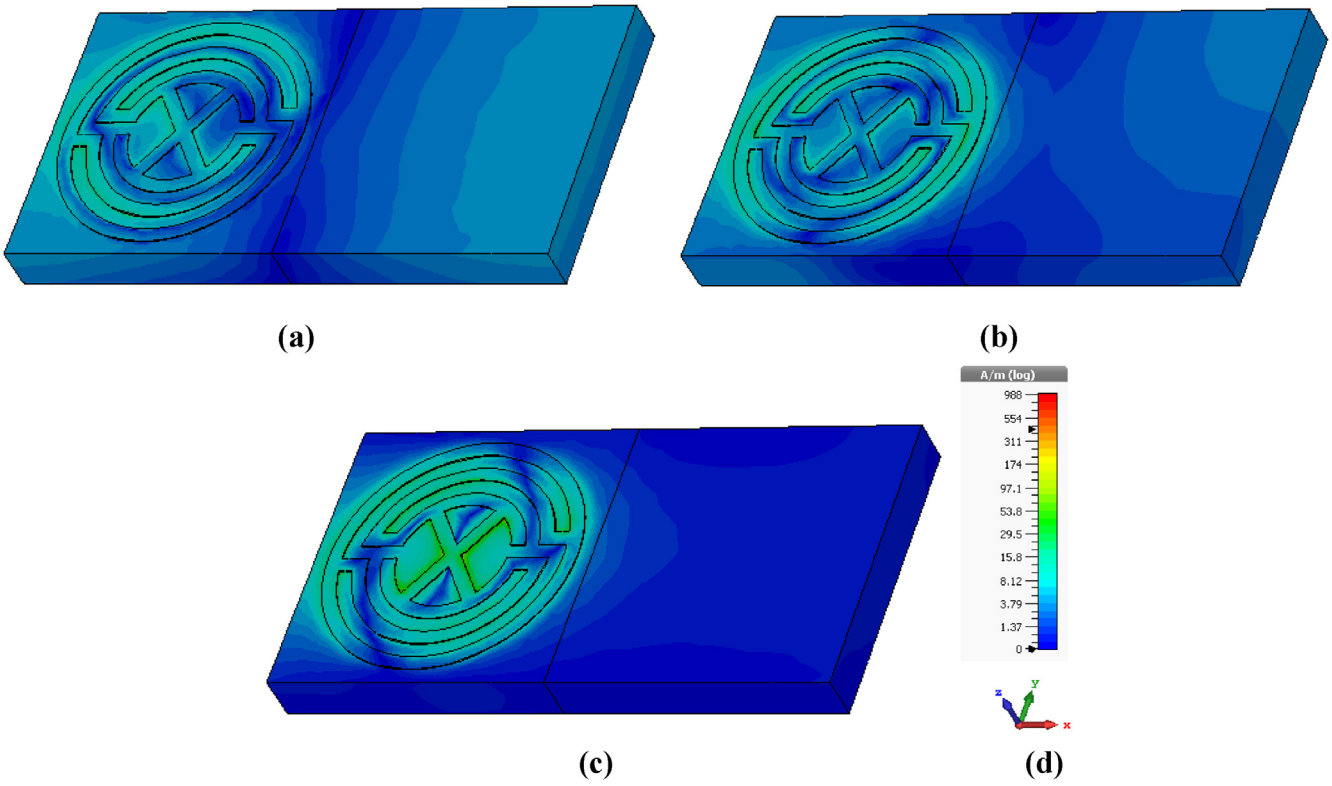

Fig. 10. Electromagnetic wave interaction on Magnetic field (a) at 6.53 GHz (b) at 10.63 GHz (c) at 13.35 GHz (d) Scale.

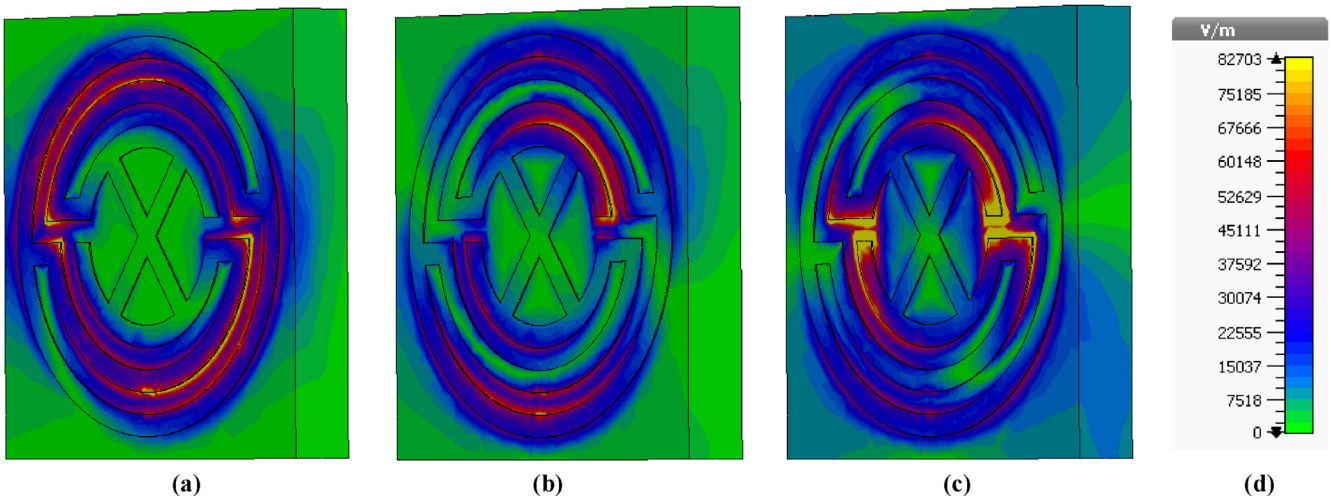

Fig. 11. Electric Field Distribution (a) 6.53 GHz (b) 10.63 GHz (c) 13.35 GHz (d) Scale.

coefficient of the X-axis port signal. Here, 5.25 GHz and 6.84 GHz are the two reflection coefficient resonance frequencies where 6.95 GHz is the transmission coefficient resonance frequency. Fig. 6(d) represents the reflection and transmission coefficient of the Y-axis port signal. It is noticeable that there are good transmission frequency bands compared to the reflection coefficient frequency bands.

Equivalent circuit and electromagnetic field analysis

Fig. 7 represents the approximate equivalent circuit of the proposed CCSRR unit cell structure. To form the proposed structure, the transmission line principle has been used the single patch element reflects the RLC circuit in series form. The relation between the resonance frequency and LC circuit can be presented by the following equation where L is lumped inductance and C is lumped capacitance.

$$f = \frac{1}{2\pi\sqrt{LC}} \tag{6}$$

When the electromagnetic wave propagates through any structure, electric and magnetic resonances are created with the combination of splits with electric field and metal loops with magnetic field. The capacitance and equivalent inductance can also be presented through the following equations where ε_0 presents free space permittivity, ε presents relative permittivity, A presents the area of the splits, d presents the split length, l is the length of the microstrip line, w is the width of the microstrip line, t is the thickness of microstrip line, correction factor, Kg is $0.57–0.145ln\frac{w}{h}$, w' represents the width of the substrate and h' represents the thickness of the substrate, respectively. The

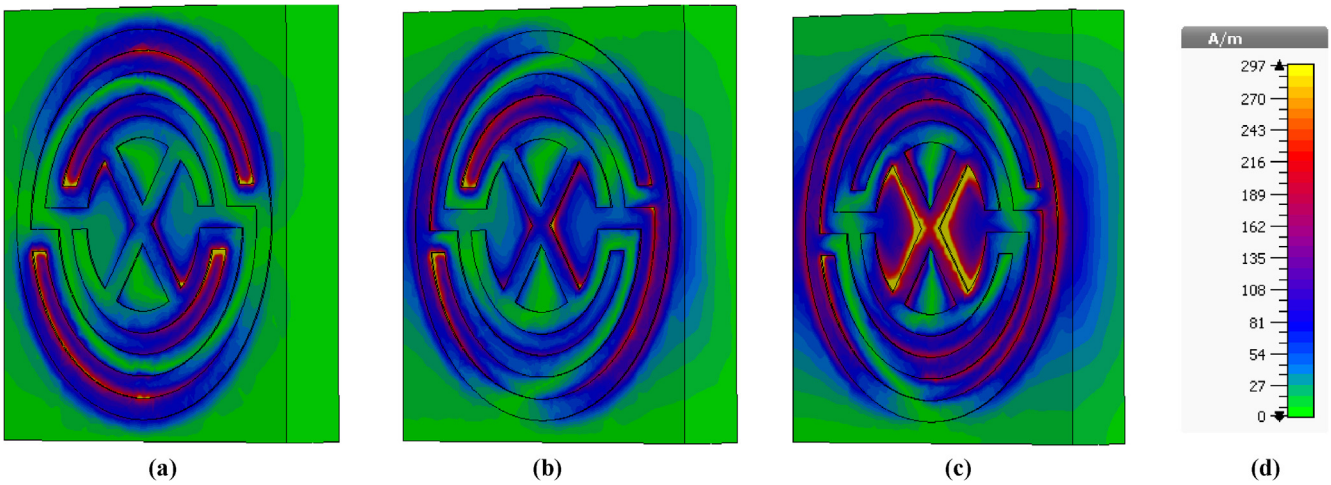

Fig. 12. Magnetic Field Distribution (a) 6.53 GHz (b) 10.63 GHz (c) 13.35 GHz (d) Scale.

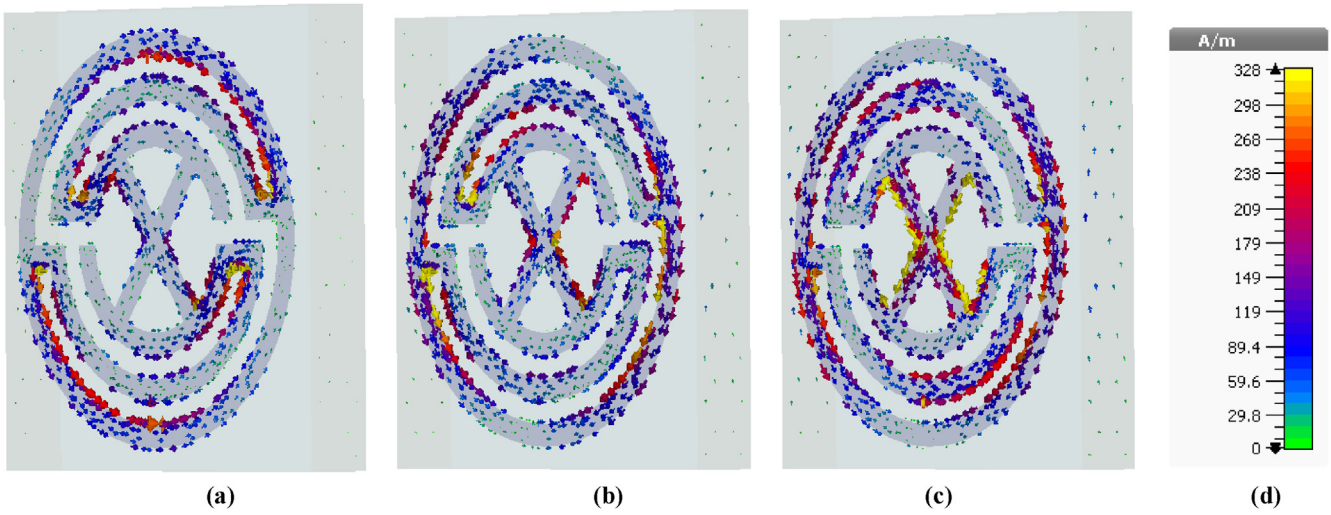

Fig. 13. Surface Current Distribution (a) 6.53 GHz (b) 10.63 GHz (c) 13.35 GHz (d) Scale.

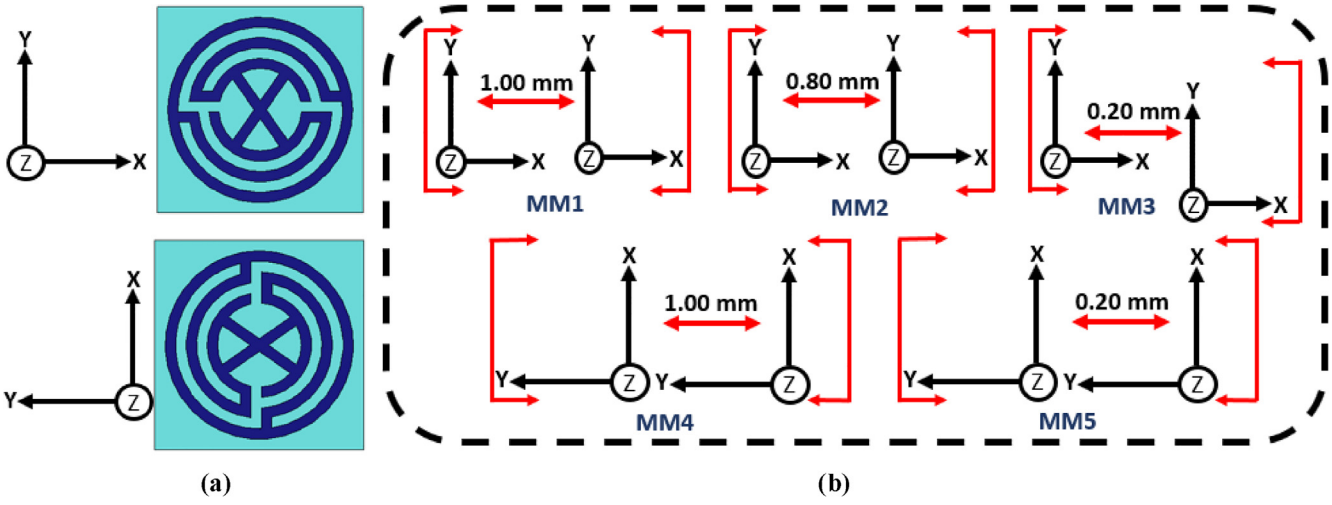

Fig. 14. (a) Axial Structure (b) Mutual Coupling on 1 × 2 array structure.

equivalent capacitance and inductance are following the concept of the transmission line principle.

$$C = \varepsilon_0 \varepsilon \frac{A}{d}(F) \tag{7}$$

$$L(nH) = 2 \times 10^{-4} l \left[\ln\left(\frac{l}{w+t}\right) + 1.193 + 0.02235\frac{w+t}{l} \right] K_g \tag{8}$$

Initial L and C magnitudes of the designed circuit were calculated based on Eqs. (7) and (8). After that, the approximated unit cell circuit

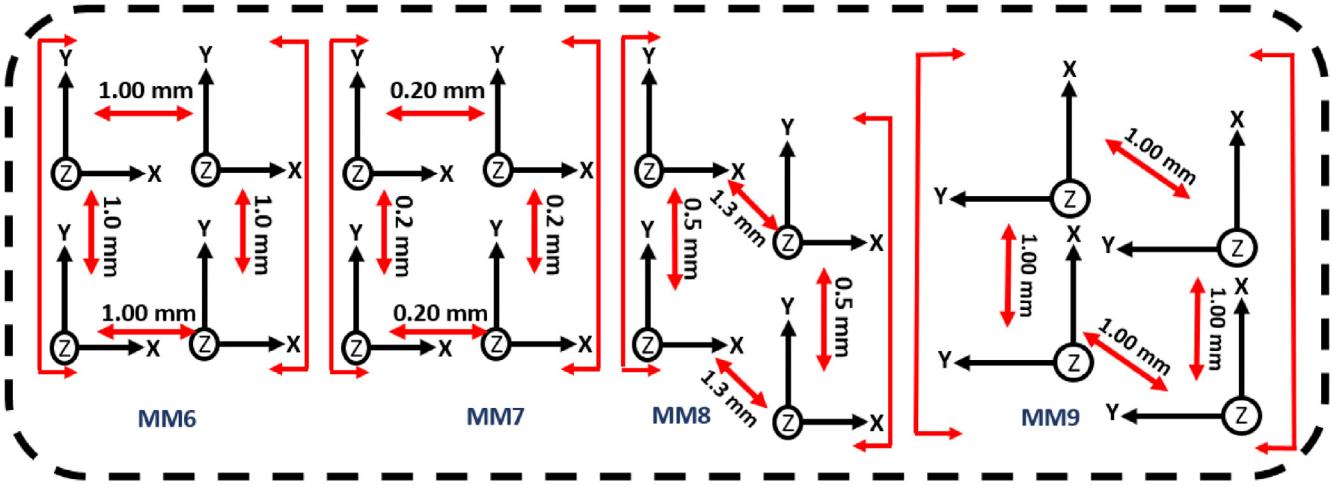

Fig. 15. Mutual Coupling on 2 × 2 array structure.

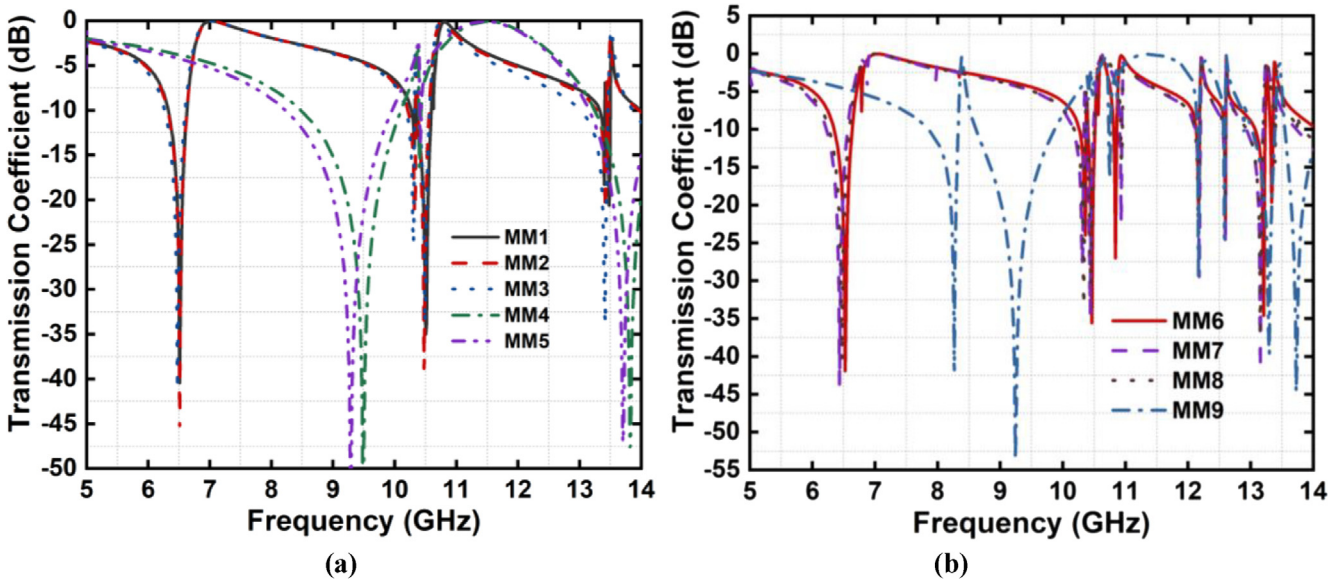

Fig. 16. Transmission Coefficient of (a) 1 × 2 array structure (b) 2 × 2 array structure.

with calculated values was designed in electromagnetic simulation software ADS for extracting the scattering parameter values. Finally, the optimized value of L and C was achieved which is shown in Fig. 7(a). The equivalent reflection coefficient is presented in Fig. 7(b) where it shows multiple resonance frequencies with good agreement although there are some deviations due to the approximation precision laggings.

In addition, the electric and magnetic field interaction is represented by the electromagnetic field which is created due to the time-varying electric charges. The constitutive parameters like effective permittivity and permeability determine the response of an incoming electromagnetic wave that can be represented by the following equations in a simple linear and isotropic medium where the permittivity (ε) and permeability (μ) are frequency-dependent in a lossless isotropic medium.

$$D = \varepsilon E \tag{9}$$

$$B = \mu H \tag{10}$$

In addition, the two constitutive relations, which describe the response of the medium to the applied fields, μ_0

$$D = \varepsilon_0 \varepsilon E \tag{11}$$

$$B = \mu_0 \mu H \tag{12}$$

The ENG-DPS interface provides non-standard electromagnetic effects like reflection and refraction of backward waves that do not exist in DPS medium. There is a maximum possibility of containing a complex structure for both single negative and double-positive media for the electromagnetic wave propagation. Artificially made lossy ENG slab is added adjacent to the natural DPS slab of Air substrate that has similar dimensions. Fig. 8 shows the ENG-DPS slab that is used to analyze through electromagnetic wave propagation. The electric and magnetic field intensity distribution for the ENG media is captured and compared with the reference DPS slab. The Electric field and magnetic field intensity for 6.53 GHz, 10.63 GHz, and 13.35 GHz, respectively are shown in Figs. 9 and 10. Negatively refracted waves in the ENG slabs and backward wave propagation have been an observing fact. It is noticeable that evanescent decaying waves are only present at the single negative medium where there is a forwarded electromagnetic wave propagation for the DPS media. The electromagnetic wave propagation inside the ENG medium is permissible, as the permittivity is negative. The refractive index will be imaginary for such kind of evanescent medium as $\varepsilon < 0$ and $\mu > 0$ which can be explained through the Drude function where Γ represents the energy dissipation factor and ω represents the frequency.

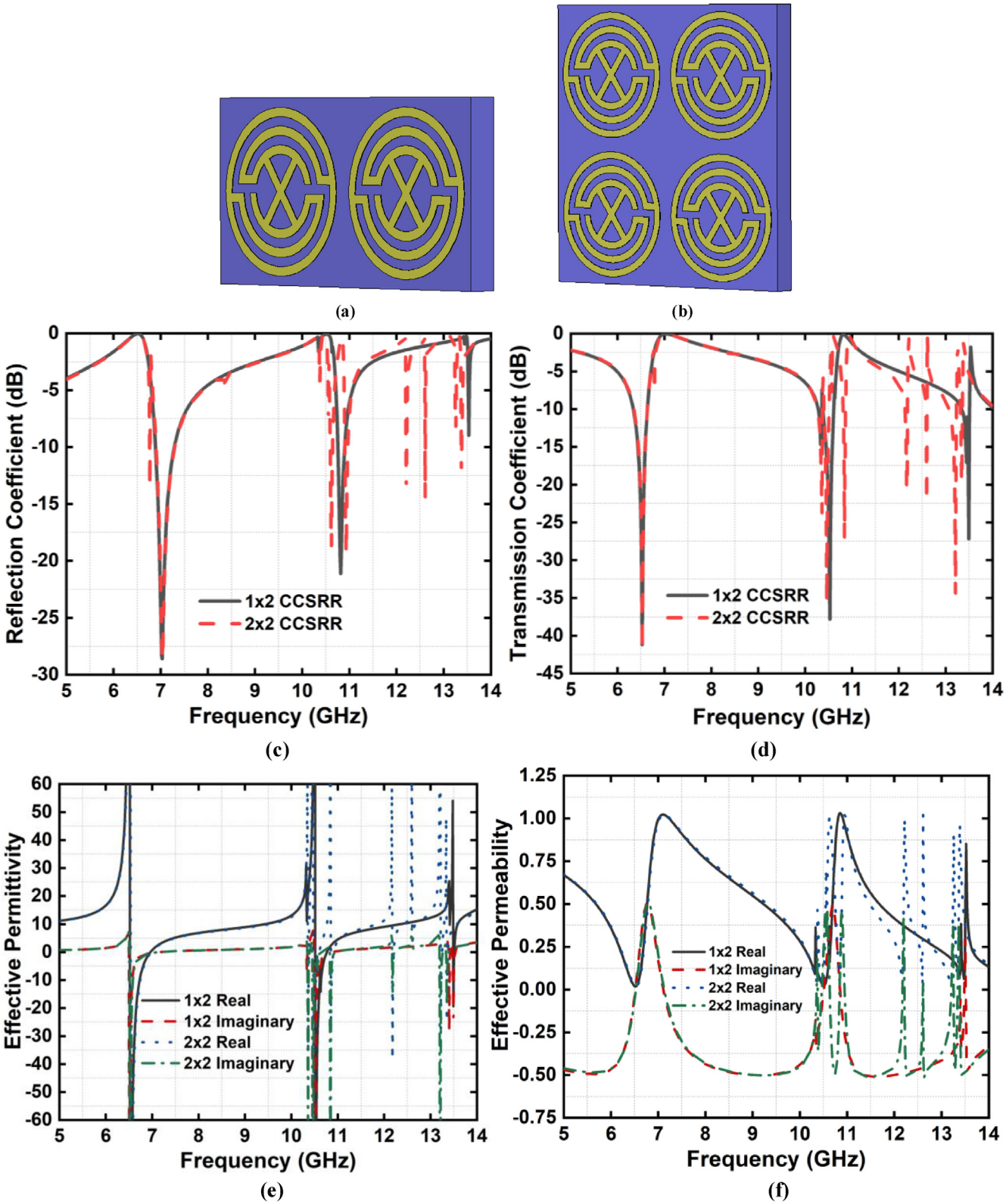

Fig. 17. (a) 1 × 2 CCSRR (b) 2 × 2 CCSRR (c) Reflection Coefficient (d) Transmission Coefficient (e) Effective Permittivity (f) Effective Permeability (g) Effective Refractive Index (h) Normalized Impedance.

$$\varepsilon(\omega) = 1 - \frac{{\omega_p}^2}{\omega(\omega + j\Gamma)} \tag{13}$$

The electric field circulations of the proposed CCSRR unit cell structure at 6.53 GHz, 10.63 GHz, and 13.35 GHz are presented in Fig. 11 that also represents the current density. The magnetic field circulations of the CCSRR metamaterial unit cell structures at 6.53 GHz, 10.63 GHz, and 13.35 GHz are presented in Fig. 12. It is observing that the current concentration is maximum at the inner central circle of the proposed structure at 6.53 GHz and it exactly shows the opposite

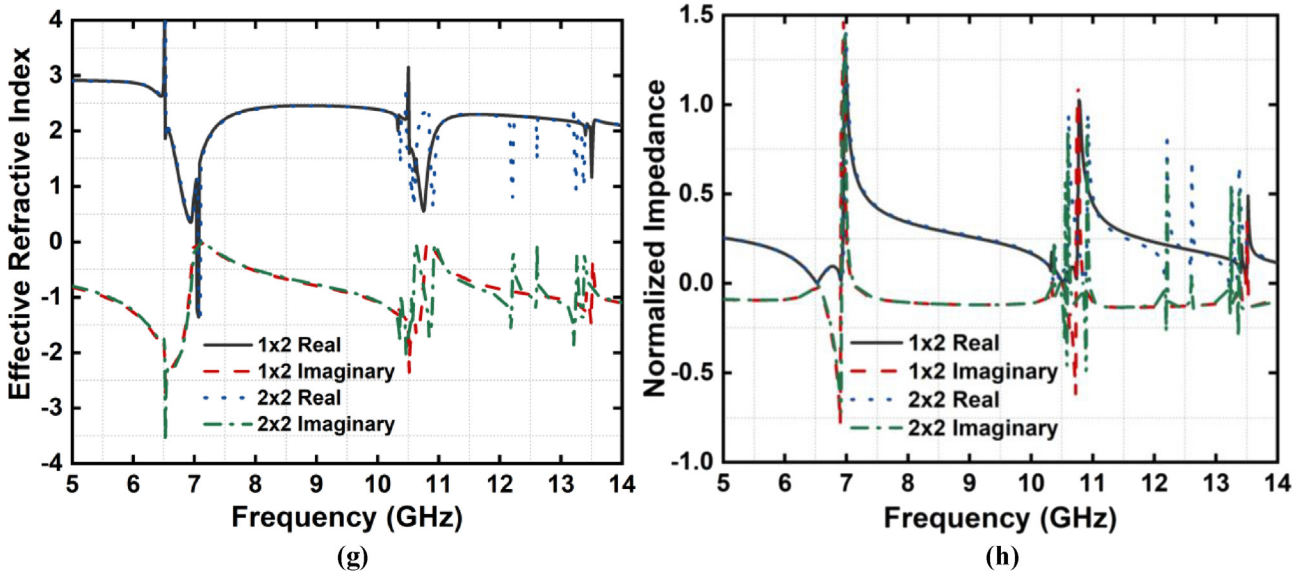

Fig. 17. (*continued*)

Table 3
Frequency ranges of imaginary effective parameters of the proposed 1 × 2 and 2 × 2 CCSRR unit cell structure.

Imaginary Parameter	Structure	Frequency Range
Negative Permittivity	1 × 2	6.48 GHz–7.11 GHz, 10.30 GHz–11.07 GHz, 13.36 GHz–13.57 GHz
Positive Permeability	1 × 2	6.50 GHz–7.11 GHz, 10.52 GHz–10.88 GHz, 13.45 GHz–13.55 GHz
Negative Permittivity	2 × 2	6.48 GHz–7.11 GHz, 10.32 GHz–10.95 GHz, 12.14 GHz–12.27 GHz, 12.58 GHz–12.62 GHz, 13.16 GHz–13.55 GHz,
Positive Permeability	2 × 2	6.50 GHz–7.11 GHz, 10.35 GHz–10.95 GHz, 12.10 GHz–12.25 GHz, 12.55 GHz–12.65 GHz, 13.18 GHz–13.43 GHz

density for the magnetic field circulation within the identical frequency regimes. For 10.63 GHz, the current density is maximum in the inner and outer circular structure in up and downside which is in the left and right outer circular structure for the magnetic field distribution. The current density is maximum at the outer side of the crossed structure for 13.35 GHz which is inside the crossed structure for magnetic field distribution. It is notable from the above analysis that all the frequencies have the opposite magnetic field distributions of the electric field distributions which meet the Maxwell equation criterion. The surface current distribution analysis is presented in Fig. 13 for the 6.53 GHz, 10.63 GHz, and 13.35 GHz, respectively. The analysis shows that the current intensity is higher at the outer structure and partially in inner structure for the 6.53 GHz where it is a similar amount for the 10.63 GHz with some partial intensity in the crossed structure. The maximum intensity has been found at the outer structure, inner structure, and the inner crossed structure for the 13.35 GHz resonance frequency.

Mutual coupling analysis

The effect on the different gap to gap intercell coupling schemes for the 1 × 2 and 2 × 2 array structure of CCSRR unit cell has been described in this section. Fig. 14(a) represents the two different axial structures of the CCSRR unit cell. Five individually identical 1 × 2 CCSRR array structures and their mutual coupling distances are presented in Fig. 14(b). MM1 and MM2 are individually identical 1 × 2 CCSRR array structures but the gap between them is different. It is noticeable that, as the separation between the two CCSRR decreases, the MM2 structure creates more distorting resonance frequencies. The coupling can also be measured by relocating the two CCSRR structures up and down shown in MM3. As MM3 is also identical to MM1, it creates the same resonance frequencies but with some distortions. MM4 and MM5 are the two different identical structures with two different distances. The coupling effect shows two different resonance frequencies which cover X-band and Ku-band, respectively. Fig. 15 represents the mutual coupling positions of four different CCSRR unit cells on the different axial structures. MM6 and MM7 are the two 2 × 2 array of CCSRR unit cells where they are positioned symmetrically. MM8 also has the symmetrical structures but the positions of the two CCSRR unit cells have up and down displacement. MM9 has the same positioning concept similar to MM8 but the axial structure is different than others. The effects are shown in Fig. 16(b). MM6 and MM7 have the same transmission frequency bands where MM8 shows almost the same frequency bands with some distortions. MM9 has multiple transmission frequencies but it covers only X-band and Ku-band. The overall analysis implies that the 1x1 and 2 × 2 CCSRR unit cell structures, which have minimum intercell structure distance, have a strong intercell coupling effect rather than the maximum intercell structure distance. Besides, the alternate axial position has performed differently compared to others. This alternate structures of MM4, MM5, or MM9 have the minimum frequency band coverage that makes the other structures acceptable for array positioning.

CCSRR unit cell array analysis

This section performs the analysis of 1 × 2 and 2 × 2 array structure of CCSRR unit cell and their scattering parameters with effective medium parameters. Fig. 17(a) and (b) represent the 1 × 2 and 2 × 2 array structures of the proposed CCSRR unit cell structures. The reflection and transmission frequencies are presented in Fig. 17(c) and (d). The reflection coefficient of the 1 × 2 CCSRR unit cell varies from 6.82 GHz to 7.32 GHz, and 10.73 GHz to 10.94 GHz, respectively where they are 6.72 GHz to 7.32 GHz, 10.55 GHz to 11.03 GHz, 12.14 GHz to 12.26 GHz, 12.55 GHz to 12.67 GHz, and 13.31 GHz to 13.43 GHz, respectively, for the 2 × 2 CCSRR unit cell structure. 1 × 2 shows the transmission coefficient frequencies from 6.31 GHz to 6.64 GHz, 10.23 GHz to 10.65 GHz, and 13.33 GHz to 13.55 GHz where they are 6.31 GHz to 6.64 GHz, 10.23 GHz to 10.65 GHz, 10.80 GHz to

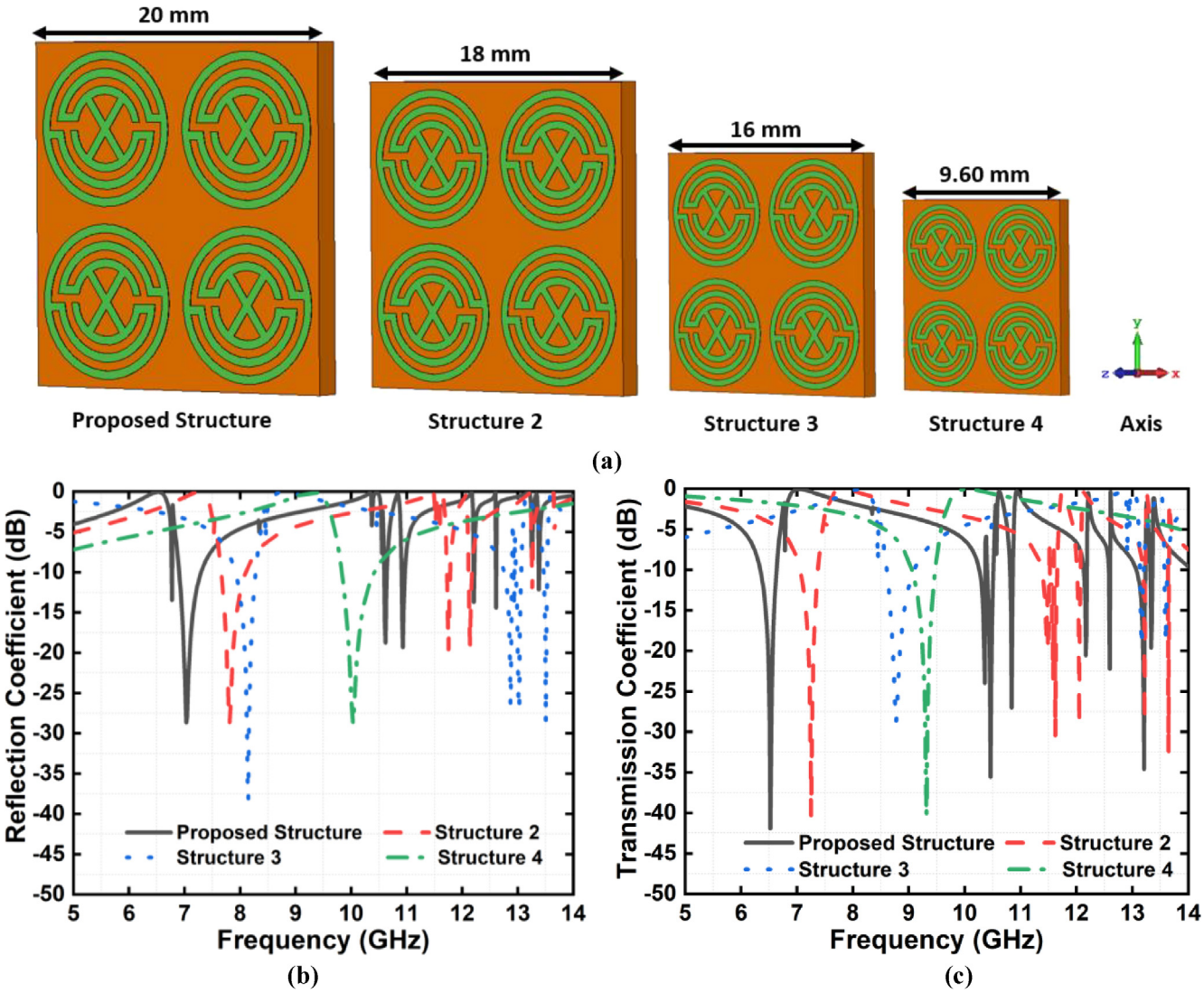

Fig. 18. Analysis of (a) Different Periodic Structures (b) Reflection Coefficient (c) Transmission Coefficient.

10.89 GHz, 12.10 GHz to 12.21 GHz, 12.54 GHz to 12.64 GHz, and 13.01 GHz to 13.50 GHz, respectively, for the 2 × 2 CCSRR unit cell structure. The effective medium parameters like permittivity, permeability, refractive index, and normalized impedance of the 1 × 2 and 2 × 2 CCSRR unit cell structures have been analyzed from Fig. 17(e) to (h). The negative real permittivity frequency ranges of 1 × 2 CCSRR unit cell structure are 6.47 GHz to 6.98 GHz, 10.46 GHz to 10.79 GHz, and 13.44 GHz to 13.55 GHz, respectively where they are 6.47 GHz to 7.25 GHz, 10.33 GHz to 10.77 GHz, and 10.77 GHz to 11.04 GHz, 12.14 GHz to 12.23 GHz, and 13.14 GHz to 13.47 GHz, respectively, for the 2 × 2 CCSRR unit cell structure. The real permeability is positive for the proposed CCSRR 1 × 2 and 2 × 2 unit cell structures. The lowest value is 0.10 for the three-resonance frequency of 6.50 GHz, 10.50 GHz, and 13.38 GHz, respectively, for the 1 × 2 CCSRR unit cell structure. 2 × 2 CCSRR unit cell structure shows multiple frequencies on the lowest permeability value of 0.10 than 1 × 2 CCSRR unit cell structure and the frequency points are 6.50 GHz, 10.50 GHz, 10.82 GHz, 12.15 GHz, 12.60 GHz, 13.22 GHz, and 13.39 GHz, respectively.

The real refractive index has the complex value in three resonance frequencies for 1 × 2 CCSRR unit cell structure where 7.08 GHz resonance point shows the value −1.35, 10.74 GHz resonance point shows the value +0.52, and 13.51 GHz resonance point shows the value +1.12, respectively. 2 × 2 CCSRR array structure has multiple resonance frequencies for the positive refractive index values but it shows the negative value of −1.35 at 7.08 GHz. The imaginary resonance frequency points for the 1 × 2 CCSRR unit cell structure are 6.54 GHz, 10.50 GHz, and 13.48 GHz where the containing values are −4.00, 2.29, and −1.41, respectively. The 2 × 2 CCSRR unit cell imaginary refractive index frequency points are 6.54 GHz, 10.50 GHz, 10.80 GHz, 12.15 GHz, 12.54 GHz, and 13.16 GHz, respectively. The normalized frequency points of 1 × 2 CCSRR unit cell structure are 6.97 GHz, and 10.76 GHz shows the impedance 1.20 Ω and 1.00 Ω where the normalized impedance is 0.48 Ω at 13.52 GHz. The imaginary normalized values are 1.5 Ω, 1.10 Ω, and 0.36 Ω for the frequency points of 6.97 GHz, 10.76 GHz, and 13.52 GHz, respectively. In addition, 2 × 2 CCSRR unit cell structure shows 1.40 Ω, 0.80 Ω, 1.00 Ω, 0.81 Ω, 0.73 Ω, 0.60 Ω, and 0.52 Ω, respectively, for the frequency points of 6.97 GHz, 10.58 GHz, 10.76 GHz, 10.93 GHz, 12.20 GHz, 12.64 GHz, and 13.36 GHz, respectively. The imaginary frequency ranges of negative permittivity and positive permeability of 1 × 2 and 2 × 2 CCSRR unit cell structures are stated in Table 3 where the standard value to evaluate is set 0. The 1 × 2 and 2 × 2 CCSRR unit cell array analysis shows that the real values are negative for the permittivity, positive for the permeability, and negative and positive both for the refractive index within the same resonance frequency bands of the proposed CCSRR unit cell structure frequency bands which indicates that 1 × 2 and 2 × 2 CCSRR unit cell also show the single

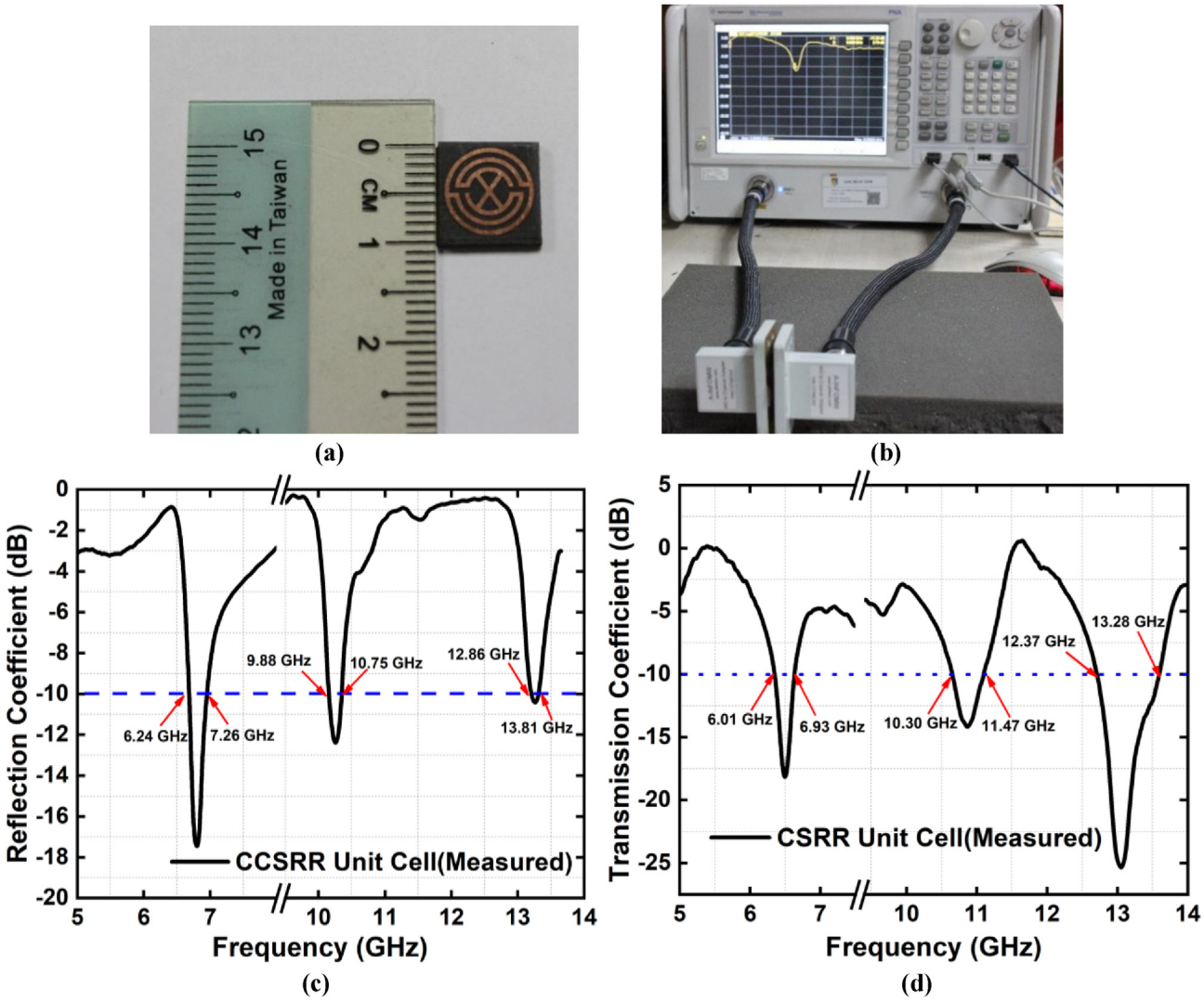

Fig. 19. (a) Fabricated prototype of the proposed CCSRR unit cell (b) Measurement setup of scattering parameters (c) Measured reflection coefficient (d) Measured transmission coefficient.

negative metamaterial characteristics.

Fig. 18 represents the different periodic structures of the proposed CCSRR unit cell 2x2 array. For the analysis purpose, four different periodic sizes have been chosen. Structure 1 represents the proposed 2x2 CCSRR unit cell array whereas the other structures are the different periodic sizes of it. The reflection coefficient of this analysis is shown in Fig. 18(a). It is noticeable that the proposed structure 1 has the maximum frequency band coverage comparing to other structures. The transmission coefficient analysis is shown in Fig. 18(b) where it is also observable that more transmission frequency bands are covered by the proposed structure 1 compare to other periodic size structures.

Results and discussion

The measurement arrangement of the proposed CCSRR unit cell has been set with the Power Network Analyzer (PNA Model N5227A). Two different waveguides (S/N J504022832 and S/N J504022826) have been used for the measurement purpose that is applied to cover frequency ranges of 5.85 GHz to 8.20 GHz and 10 GHz to 15 GHz. Fig. 19(a) shows the fabricated prototype of the single and 2x2 CCSRR unit cell structure with the measurement setup shown in Fig. 19(b). The reflection and transmission coefficient of the proposed CCSRR unit cell structure has been shown in Fig. 19(c) and (d), respectively. The frequency ranges for the measured reflection coefficient are 6.24 GHz to 7.26 GHz, 9.88 GHz to 10.75 GHz, and 12.86 GHz to 13.81 GHz, respectively. In addition, the measured operating transmission frequency ranges are 6.01 GHz to 6.93 GHz, 10.30 GHz to 11.47 GHz, and 12.37 GHz to 13.28 GHz, respectively.

Fig. 20(a) represents the measurement setup and 18x20 array structure of the proposed CCSRR unit cell. The array structure has been set inside the anechoic chamber in between of two horn antennas. The distance of the two horn antennas is set 180 mm. The horn antennas are connected with the PNA to measure the reflection and transmission coefficient of the proposed CCSRR unit cell array structure. Fig. 20(b) and (c) show the reflection and transmission coefficient of the array structure. The wave propagates towards the z-directions for the normal incidences. The array prototype shows the good agreement with the simulation results altough there are multiple resonace frequencies in the measurement results which are the results of the mutual coupling effects of the unit cell structures.

One of the important factors in the metamaterial research area is the effective medium ratio (EMR). The EMR represents the compactness and effectiveness of the metamaterial. Eq. (14) represents the EMR extraction formula.

$$EMR = \frac{\lambda}{L} \tag{14}$$

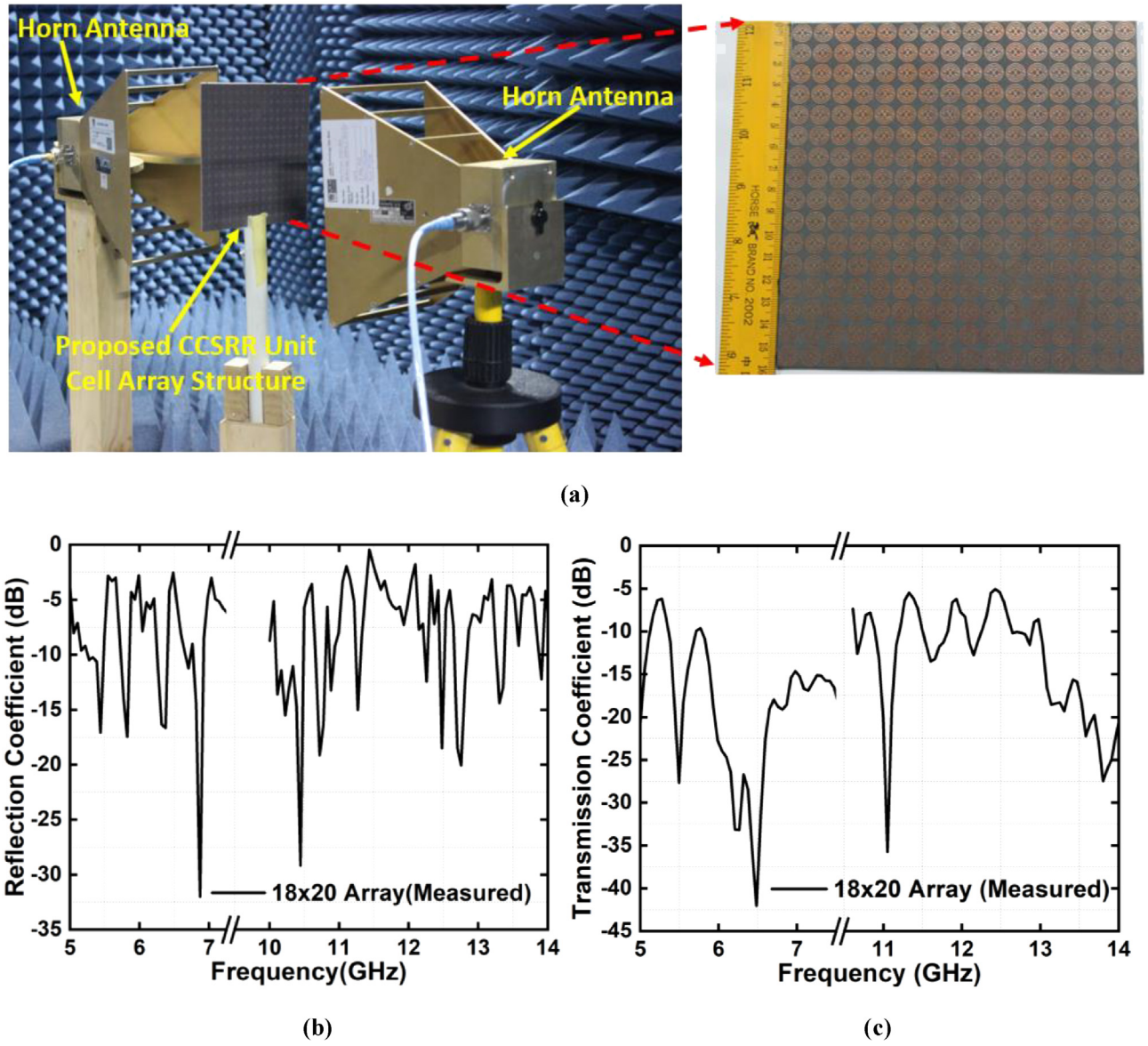

Fig. 20. (a) Measurement setup with the fabricated CCSRR unit cell array prototype (b) Measured reflection coefficient (c) Measured transmission coefficient.

Table 4
Comparison of proposed CCSRR unit cell and existing metamaterial unit cell.

References	Unit Cell Shape	Dimensions (mm^2)	Frequency Bands	EMR	Remarks of Proposed
[29]	Modified Z-shaped	10 × 10	X-band	4	Maximum Bands, High EMR
[30]	Double C-shaped	12 × 12	S-band, C-band, X-band	7.44	Compressed Size
[12]	Complementary SRR	5.5 × 5.5	C-band	8.0	Maximum Bands
[31]	S-shaped	8.5 × 8.5	X-band	2.09	Maximum Bands, High EMR
[32]	Resistor loaded sector-shaped	12.5 × 12.5	C-band, X-band	N/A	Maximum Bands, Compressed Size
[33]	Modified H-shaped	9 × 9	X-band, Ku-band	3	Maximum Bands, High EMR
[34]	Ultra-thin compact	6.1 × 6.1	X-band	N/A	Maximum Bands
[35]	S-shaped	10 × 10	X-band	2.4	Maximum Bands, High EMR
[36]	Circular	5 × 5	X-band	8.45	Maximum Bands
[37]	SRR	5 × 5	X-band	6.51	Maximum Bands
[11]	Hexagonal	10 × 10	S-band, X-band	8.4	Maximum Bands
[38]	Inverse Double L-shaped	10 × 10	C-band, X-band, and Ku-band	3.9	High EMR
[39]	Four-fold symmetry	7 × 7	X-Band	N/A	Maximum Bands
[40]	Four-fold symmetry	28.2 × 28.2	C-Band	N/A	Maximum Bands, Compressed Size
[41]	Circular sector	9 × 9	C-Band	N/A	Maximum Bands
[42]	Nickel concentrated	25 × 20	X-band, Ku-band	N/A	Maximum Bands, Compressed Size
[15]	U-joint double spilt O shaped	15 × 12	X-band, Ku-Band	4.5	Maximum Bands, Compressed Size
[16]	Circular and square	**8 × 8**	C-band, Ku-band	3.264	Maximum Bands, High EMR
Proposed	**Concentric Crossed Line**	**10 × 10**	**C-band, X-band, and Ku-band**	**4.5**	**Single Negative Metamaterial Characteristics**

λ: wavelength and L: CCSRR unit cell dimension.

The EMR of the proposed CCSRR unit cell is 4.5 for $10 \times 10 \times 1.575$ mm^3 dimension in with the frequency of 6.53 GHz. The EMR value 4.5 of the proposed unit cell expands its consistency and decreases its electrical dimensions without any fabrication restrictions. The proposed CCSRR unit cell structure among the existing unit cell structures and their comparison are presented in Table 4. The analysis shows that the proposed CCSRR unit cell structure covers the tri-band frequencies with single negative metamaterial characteristics.

Conclusion

Design and experimental analysis of a metamaterial based on an epsilon negative unit cell have been performed in this paper. A numerical analysis has also been performed for the unit cell and its array structures. The proposed unit cell structure comprises concentric crossed line SRR with an electrical dimension of $0.22\lambda \times 0.22\lambda$ at 6.53 GHz. The region of the single negative characteristics for the proposed CCSRR unit cell structure has been found from 6.53 GHz to 6.96 GHz, 10.63 GHz to 10.91 GHz, and 13.37 GHz to 13.40 GHz, respectively that makes the propagation reversed where the radiations get bent backward to its structure and allow it to be appropriate for various microwave applications. The effective medium parameters have been carried out by performing parametric studies on different length and width with different structures. The designed metamaterial shows single negative characteristics at C-band, X-band and Ku-band respectively. The EMR value of 4.5 implies the compactness and design flexibility for practical microwave applications. Thus, the proposed metamaterial can be a solution in satellite communications, navigation beacons, and optical communications of the microwave frequency regime.

Funding

This research is funded by Universiti Kebangsaan Malaysia Research grant GUP-2020-074. The project was funded by the Deanship of Scientific Research (DSR), King Abdulaziz University, Jeddah, Saudi Arabia under grant no. KEP-24-135-38. The authors, therefore, acknowledge with thanks to DSR technical and financial support.

CRediT authorship contribution statement

Mohammad Shahidul Islam: Conceptualization, Data curation, Formal analysis, Investigation, Software, Writing - original draft, Writing - review & editing. **Mohammad Tariqul Islam:** Conceptualization, Data curation, Methodology, Formal analysis, Funding acquisition, Investigation, Software, Supervision, Visualization, Writing - review & editing. **Norsuzlin Mohd Sahar:** Formal analysis. **Hatem Rmili:** Funding acquisition, Software, Writing - review & editing. **Nowshad Amin:** Funding acquisition, Writing - review & editing, Methodology. **Muhammad E.H. Chowdhury:** Software, Writing - review & editing.

Declaration of Competing Interest

The authors declare that they have no known competing financial interests or personal relationships that could have appeared to influence the work reported in this paper.

References

[1] Deshmukh R, Marathe D, Kulat KD. Design of multiband negative permittivity metamaterial based on interdigitated and meander line resonator. 25th National Conference on Communications, NCC 2019. 2019.
[2] Dhar N, Rahman MA, Hossain MA. Design and exploration of functioning of a D-Z shaped SNG multiband metamaterial for L-, S-, and X-bands applications. SN Appl Sci 2020;2(6):1077.
[3] Singh H, Mittal N, Arora O. Designing and analysis of frequency reconfigurable double negative flower leaf metamaterial resonator. Mater Today: Proc 2020.
[4] Misran N, Islam MT, Ismail MY, Yusop SH. Analisis pencirian parameter ketebalan dan kebertelusan substrat bagi elemen cincin segiempat sepusat bersela antena tatasusun pantulan. J Kejuruter 2011;23(November):11–5.
[5] Sabah C. Novel, dual band, single and double negative metamaterials: noncon-centric delta loop resonators. Prog. Electromagn. Res. 2010;25(September):225–39.
[6] Hossain TM, et al. Bandwidth enhancement of five-port reflectometer-based ENG DSRR metamaterial for microwave imaging application. Sensors Actuators, A Phys 2020;303:111638.
[7] Islam SS, Khan MS, Faruque MRI. Design and analysis of modified- split H-shaped DNG metamaterial for microwave application. Mater Res Express 2019;6(10):105356.
[8] Nguyen TQH, Nguyen TKT, Cao TN, Nguyen H, Bach LG. Numerical study of a broadband metamaterial absorber using a single split circle ring and lumped resistors for X-band applications. AIP Adv 2020;10(3):035326.
[9] Pandit S, Mohan A, Ray P. Dual-band negative-permittivity metamaterial using crossed loop resonator. Appl Phys A Mater Sci Process 2019;125(6):1–6.
[10] Dai Ji, Luo H, Moloney M, Qiu J. Adjustable graphene/polyolefin elastomer epsilon-near-zero metamaterials at radiofrequency range. ACS Appl Mater Interfaces 2020;12(19):22019–28.
[11] Shahidul Islam M, Samsuzzaman Md, Beng GK, Misran N, Amin N, Islam MT. A Gap coupled hexagonal split ring resonator based metamaterial for S-band and X-band microwave applications. IEEE Access 2020;8.
[12] Almutairi AF, Islam MS, Samsuzzaman M, Islam MT, Misran N, Islam MT. A complementary split ring resonator based metamaterial with effective medium ratio for C-band microwave applications. Results Phys. 2019;15(July):102675.
[13] Ahamed E, Faruque MRI, Bin Mansor MF, Islam MT. Polarization-dependent tunneled metamaterial structure with enhanced fields properties for X-band application. Results Phys 2019;15:102530.
[14] Ramachandran T, Faruque MRI, Ahamed E, Abdullah S. Specific absorption rate reduction of multi split square ring metamaterial for L- and S-band application. Results Phys 2019;15:102668.
[15] Hoque A, Islam MT, Almutairi AF, Faruque MRI, Singh MJ, Islam MS. U-joint Double split O (UDO) shaped with split square metasurface absorber for X and ku band application. Results Phys 2019;15:102757.
[16] Ramachandran T, Faruque MRI, Islam MT. A dual band left-handed metamaterial-enabled design for satellite applications. Results Phys 2020;16:102942.
[17] Cheng Y, Li W, Mao X. Triple-band polarization angle independent 90° polarization rotator based on fermat's spiral structure planar chiral metamaterial. Prog Electromagn Res 2019;165:35–45.
[18] Cheng Y, Fan J, Luo H, Chen F. Dual-band and high-efficiency circular polarization convertor based on anisotropic metamaterial. IEEE Access 2020;8:7615–21.
[19] Wang Q, Cheng Y. Compact and low-frequency broadband microwave metamaterial absorber based on meander wire structure loaded resistors. AEU - Int J Electron Commun 2020;120:153198.
[20] Cheng Y, Luo H, Chen F. Broadband metamaterial microwave absorber based on asymmetric sectional resonator structures. J Appl Phys 2020;127(21):214902.
[21] Cheng Y, Zou Y, Luo H, Chen F, Mao X. Compact ultra-thin seven-band microwave metamaterial absorber based on a single resonator structure. J Electron Mater 2019;48(6):3939–46.
[22] Cheng Y, Cheng Z, Mao X, Gong R. Ultra-thin multi-band polarization-insensitive microwave metamaterial absorber based on multiple-order responses using a single resonator structure. Materials (Basel) 2017;10(11):1241.
[23] Roy Chowdhury D, Singh R, Taylor AJ, Chen H-T, Zhang W, Azad AK. Coupling schemes in terahertz planar metamaterials. Int. J. Optics 2012;2012.
[24] Pung AJ, Goldflam MD, Burckel DB, Brener I, Sinclair MB, Campione S. Enhancing absorption bandwidth through vertically oriented metamaterials. Appl. Sci. 2019;9(11):2223.
[25] Al-Naib I, Hebestreit E, Rockstuhl C, Lederer F, Christodoulides D, Ozaki T, Morandotti R. Conductive coupling of split ring resonators: a path to THz metamaterials with ultrasharp resonances. Phys Rev Lett 2014;112(18).
[26] Singh R, Rockstuhl C, Zhang W. Strong influence of packing density in terahertz metamaterials. Appl Phys Lett 2010;97(24):241108.
[27] Wallauer J, Bitzer A, Waselikowski S, Walther M. Near-field signature of electromagnetic coupling in metamaterial arrays: a terahertz microscopy study. Opt Express 2011;19(18):17283.
[28] Luukkonen O, Maslovski SI, Tretyakov SA. A stepwise nicolson–ross–weir-based material parameter extraction method. IEEE Antennas Wirel Propag Lett 2011;10:1295–8.
[29] Hasan MM, Faruque MRI, Islam SS, Islam MT. A new compact double-negative miniaturized metamaterial for wideband operation. Materials (Basel) 2016;9(10):1–12.
[30] Hossain MJ, Faruque MRI, Islam MT. Design and analysis of a new composite double negative metamaterial for multi-band communication. Curr Appl Phys 2017;17(7):931–9.
[31] Zhou Z, Yang H. Triple-band asymmetric transmission of linear polarization with deformed S-shape bilayer chiral metamaterial. Appl Phys A 2015;119(1):115–9.
[32] Kalraiya S, Chaudhary RK, Abdalla MA. Design and analysis of polarization independent conformal wideband metamaterial absorber using resistor loaded sector shaped resonators. J Appl Phys Apr. 2019;125(13):134904.
[33] Hossain TM, Jamlos MF, Jamlos MA, Soh PJ, Islam MI, Khan R. Modified H-shaped DNG metamaterial for multiband microwave application. Appl Phys A 2018;124(2). https://doi.org/10.1007/s00339-018-1593-6.
[34] Kumari K, Mishra N, Chaudhary RK. An ultra-thin compact polarization insensitive

dual band absorber based on metamaterial for X-band applications. Microw Opt Technol Lett Oct. 2017;59(10):2664–9.
[35] Hasan MM, Faruque MRI, Islam MT. Parametric studies on split S-shaped composite meta atom for X-band communication. Bull Polish Acad Sci Tech Sci 2017;65(4):533–9.
[36] Liu SH, Guo LX, Li JC. Left-handed metamaterials based on only modified circular electric resonators. J Mod Opt 2016;63(21):2220–5.
[37] Liu P, Yang S, Jain A, Wang Q, Jiang H, Song J, Koschny T, Soukoulis CM, Dong L. Tunable meta-atom using liquid metal embedded in stretchable polymer. J Appl Phys 2015;118(1).
[38] Tamim AM, Faruque MRI, Alam MJ, Islam SS, Islam MT. Split ring resonator loaded horizontally inverse double L-shaped metamaterial for C-, X- and K u -Band Microwave applications. Results Phys 2019;12:2112–22.
[39] Thummaluru SR, Mishra N, Chaudhary RK. Design and analysis of an ultrathin X-band polarization-insensitive metamaterial absorber. Microw Opt Technol Lett 2016;58(10):2481–5.
[40] Thummaluru SR, Mishra N, Chaudhary RK. Design and analysis of an ultrathin triple-band polarization independent metamaterial absorber. AEU – Int. J. Electron. Commun. 2017;82:508–15.
[41] Thummaluru SR, Chaudhary RK. Polarization controllable and wide-angle frequency tunable metamaterial absorber. J Appl Phys Nov. 2018;124(20):204901.
[42] Faruque MRI, Ahamed E, Rahman MA, Islam MT. Flexible nickel aluminate (NiAl2O4) based dual-band double negative metamaterial for microwave applications. Results Phys Sep. 2019;14:102524.